

**Simultaneous Alignment and Figure Testing of Optical System Components via
Aberration Measurement and Reverse Optimization**

by

Mark Andrew Lundgren

A Dissertation Submitted to the Faculty of the
COMMITTEE ON OPTICAL SCIENCES (GRADUATE)

In Partial Fulfillment of the Requirements
For the Degree of

DOCTOR OF PHILOSOPHY

In the Graduate College

THE UNIVERSITY OF ARIZONA

1990

INFORMATION TO USERS

The most advanced technology has been used to photograph and reproduce this manuscript from the microfilm master. UMI films the text directly from the original or copy submitted. Thus, some thesis and dissertation copies are in typewriter face, while others may be from any type of computer printer.

The quality of this reproduction is dependent upon the quality of the copy submitted. Broken or indistinct print, colored or poor quality illustrations and photographs, print bleedthrough, substandard margins, and improper alignment can adversely affect reproduction.

In the unlikely event that the author did not send UMI a complete manuscript and there are missing pages, these will be noted. Also, if unauthorized copyright material had to be removed, a note will indicate the deletion.

Oversize materials (e.g., maps, drawings, charts) are reproduced by sectioning the original, beginning at the upper left-hand corner and continuing from left to right in equal sections with small overlaps. Each original is also photographed in one exposure and is included in reduced form at the back of the book.

Photographs included in the original manuscript have been reproduced xerographically in this copy. Higher quality 6" x 9" black and white photographic prints are available for any photographs or illustrations appearing in this copy for an additional charge. Contact UMI directly to order.

U·M·I

University Microfilms International
A Bell & Howell Information Company
300 North Zeeb Road, Ann Arbor, MI 48106-1346 USA
313/761-4700 800/521-0600



Order Number 9114062

**Simultaneous alignment and figure testing of optical system
components via aberration measurement and reverse
optimization**

Lundgren, Mark Andrew, Ph.D.

The University of Arizona, 1990

U·M·I

300 N. Zeeb Rd.
Ann Arbor, MI 48106



**Simultaneous Alignment and Figure Testing of Optical System Components via
Aberration Measurement and Reverse Optimization**

by

Mark Andrew Lundgren

A Dissertation Submitted to the Faculty of the
COMMITTEE ON OPTICAL SCIENCES (GRADUATE)

In Partial Fulfillment of the Requirements
For the Degree of

DOCTOR OF PHILOSOPHY

In the Graduate College

THE UNIVERSITY OF ARIZONA

1990

THE UNIVERSITY OF ARIZONA
GRADUATE COLLEGE

As members of the Final Examination Committee, we certify that we have read
the dissertation prepared by Mark A. Lundgren

entitled Simultaneous Alignment and Figure Testing of Optical System
Components via Aberration Measurement and Reverse Optimization

and recommend that it be accepted as fulfilling the dissertation requirement
for the Degree of Doctor of Philosophy.

Tom J. Malvern

12/13/90
Date

W. W. White

11/13/90
Date

George N. Coen

11/13/90
Date

Date

Date

Final approval and acceptance of this dissertation is contingent upon the
candidate's submission of the final copy of the dissertation to the Graduate
College.

I hereby certify that I have read this dissertation prepared under my
direction and recommend that it be accepted as fulfilling the dissertation
requirement.

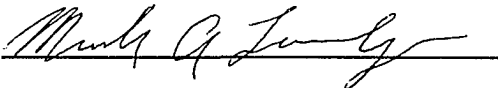
W. W. White 11/13/90
Dissertation Director

Date

STATEMENT BY AUTHOR

This dissertation has been submitted in partial fulfillment of requirements for an advanced degree at The University of Arizona and is deposited in the University Library to be made available to borrowers under rules of the Library.

Brief quotations from this dissertation are allowable without special permission, provided that accurate acknowledgment of source is made. Requests for permission for extended quotation from or reproduction of this manuscript in whole or in part may be granted by the head of the major department or the Dean of the Graduate College when in his or her judgment the proposed use of the material is in the interests of scholarship. In all other instances, however, permission must be obtained from the author.

SIGNED: 

ACKNOWLEDGMENTS

I would first like to thank Bill Wolfe, my advisor, for his support, direction, and patience. I would also like to thank George Lawrence for his help with the three-mirror project and for serving on my committee, and Tom Milster, my third committee member. Thanks to Anne Damon, Vic Sinclair, Lang Brod, Ken Johnson, and many other people who helped out when I needed it. Thanks to Dave Himlin and John Weis of Rockwell International for their help and support, and to Kie Nahm, Hwan Joo Jeong, and Gordon Videen who contributed to this effort. Thanks to Tom Heydenburg and Bill Griffin of Wally J. Shafer and Kevin Magde of RADC for their help with the OPTECAL. Last, I would like to thank my parents, Arthur and Ruth Lundgren, whose love and encouragement made all the years of school and the writing of this dissertation possible.

TABLE OF CONTENTS

	Page
LIST OF ILLUSTRATIONS.....	6
LIST OF TABLES.....	8
ABSTRACT.....	11
1. INTRODUCTION.....	13
2. RAY ABERRATION METHOD.....	18
3. INTRODUCTION TO WAVEFRONT ABERRATION MEASUREMENT IN REVERSE OPTIMIZATION.....	35
4. CASSEGRAINIAN TELESCOPE.....	40
5. COOKE TRIPLET.....	48
6. SIMULATION WITH TWO-PETZVAL TELESCOPE.....	61
7. EFFECTS OF GAUSSIAN NOISE ON THE OPTIMIZATION PROCESS.....	80
8. EXPERIMENTAL VERIFICATION.....	85
9. CONCLUSION.....	97
 APPENDIX A. REVIEW OF OPTIMIZATION.....	 101
APPENDIX B. SOFTWARE FOR NOISE SIMULATION.....	103
APPENDIX C. OPTIMIZATION TECHNIQUES.....	105
REFERENCES.....	109

LIST OF ILLUSTRATIONS

	Page
2.1 Three-mirror test-bench with collimated light-source, Hartmann screen and suspended shutter-plate.....	20
2.2 The Hartmann screen defines the chief-rays and is therefore located at the entrance pupil.....	25
2.3 Position sensing detector.....	25
2.4 Operating system schematic.....	26
2.5 Mirror adjustments during alignment.....	28
2.6 Alignment improvement vs. iteration.....	30
3.1 Zernike coefficients for deformations and misalignments.....	36
4.1 Cassegrainian telescope.....	43
4.2 MTF's of nominal, misaligned, and realigned Cassegrainian telescope.....	44
4.3 Fields and coordinates.....	46
4.4 Rays used in optimizations.....	46
5.1 Cooke triplet.....	50
5.2 Nominal triplet performance.....	51
5.3 Misaligned triplet performance.....	51
5.4 Realigned triplet performance.....	51
5.5 Performance of triplet optimized with mismodelling.....	51
5.6 Performance of triplet realigned with 6 figure variables.....	51
5.7 Performance of triplet realigned with 4 figure variables.....	51
6.1 Two-Petzval telescope.....	62
6.2 Nominal two-Petzval performance.....	65
6.3 Misaligned two-Petzval performance.....	65

6.4	Realigned two-Petzval performance.....	65
6.5	Rays used in optimization.....	67
6.6	Initial deformation surface 15, contour.....	70
6.7	Initial deformation, surface 15, 3-D.....	70
6.8	Optimized surface 15, contour.....	71
6.9	Optimized surface 15, 3-D.....	71
6.10	Optimized surface 15 with misalignments, contour.....	72
6.11	Optimized surface 15 with misalignments, 3-D.....	72
6.12	Rayset for optimization.....	76
6.13	Initial deformation, surface 15, contour.....	77
6.14	Initial deformation, surface 15, 3-D.....	77
6.15	Initial deformation, surface 35, contour.....	77
6.16	Initial deformation, surface 35, 3-D.....	77
6.17	Optimized surface 15, contour.....	78
6.18	Optimized surface 15, 3-D.....	78
6.19	Optimized surface 35, contour.....	78
6.20	Optimized surface 35, 3-D.....	78
7.1	Effects of noise on optimization.....	82
7.2	Effects of noise and target number on realigned performance.....	82
8.1	OPTECAL schematic diagram showing Zygo interferometer as light-source, the collimating and imaging parabolas, and the fold mirrors.....	86
8.2	Simulating tilt and piston.....	89
8.3-5	Simulated two-Petzval nominal interferograms.....	91

8.6-8	OPTECAL interferograms.....	91
8.9	Optimization, case 1.....	93
8.10	Optimization, case 2.....	96

LIST OF TABLES

	Page
4.1 Prescription of Cassegrainian telescope.....	44
4.2 Tolerancing of Cassegrainian telescope.....	44
4.3 Optimization of Cassegrainian telescope.....	46
5.1 Prescription of Cooke triplet.....	49
5.2 Cooke triplet tolerances.....	49
5.3 Realignment of triplet, misalignments only.....	53
5.4 Performance of triplet, misalignments only.....	53
5.5 Modelling errors in triplet.....	54
5.6 Results of reverse optimization with severe modelling errors.....	55
5.7 Performance of system optimized with severe modelling errors.....	55
5.8 Results of optimization with mismodelling and variable curvatures.....	56
5.9 Performance of system optimized with mismodelling and variable curvatures.....	57
5.10 Curvature optimization, case 1.....	57
5.11 Results of reverse optimization with variable curvatures, case 2.....	58
5.12 Curvature optimization, case 2.....	59
5.13 Performance of system optimized with variable curvatures, case 2.....	59
6.1 Prescription of two-Petzval telescope.....	63
6.2 Performance of two-Petzval telescope.....	64
6.3 Misalignments of two-Petzval telescope.....	66
6.4 Performance of misaligned two-Petzval telescope.....	67
6.5 Realignment of two-Petzval telescope.....	69
6.6 Performance of realigned two-Petzval telescope.....	69
6.7 Realignment with 1 surface deformation.....	74

6.8	Performance of realigned telescope with one surface deformation.....	74
6.9	Optimization of misalignments and two surface deformations.....	76
6.10	Performance of realigned telescope with deformations.....	76
8.1	Optimization of nominal misalignments.....	90
8.2	Nominal RMS wavefront error of OPTECAL.....	92
8.3	Optimization of OPTECAL, case 1.....	93
8.4	New nominal state.....	94
8.5	Optimization of OPTECAL, case 2.....	95
C.1	Targets for optimization.....	105
C.2	Rayset for AccosV.....	106
C.3	Rayset for OSLO.....	108

ABSTRACT

Optical component alignment and testing using reverse optimization has been investigated for different measurement methods and optical systems. The methods discussed were ray aberration measurement and wavefront aberration measurement. The methods were applied to real and simulated optical systems and compared.

A testbed was designed to measure ray aberrations by means of physical raytracing of a three-mirror telescope in order to align the telescope by means of ray aberration measurement and reverse optimization, a technique of computer aided alignment. Ray aberration measurements were used to align the three-mirror telescope. Experimental results and improvements to the technique are discussed.

Wavefront aberration methods are described and compared to ray aberration measurements. The wavefront aberration method was more easily used with systems with low nominal aberrations and when figure testing is desired. The ray aberration technique is most useful with systems of large aberration when capture range may be a problem and when component figure is well known.

The method of reverse optimization is shown to work for wavefront aberration measurements in computer simulations using a Cassegrainian telescope, Cooke triplet and afocal two-Petzval telescope.

Component figure errors and misalignments were determined simultaneously with sufficient spatial sampling of the wavefront aberrations. Surface parameters and component alignments were used as optimization variables.

The effects of gaussian noise on the wavefront data were simulated for misalignment of the two-Petzval design. Results showed that noise can be compensated by the use of large numbers of optimization targets.

Wavefront aberration measurements and reverse optimization were used to align a laboratory two-Petzval system to verify the results of the simulations.

CHAPTER 1

INTRODUCTION

1.1 Motivation

In the last few years, demand has increased for wide field of view, large stray light rejection, high resolution telescopes. With the aid of computer grinding and polishing techniques, off-axis and aspheric elements have come into wide use in this field. High quality lenses with many elements have also become more important to industry in the field of photo-etching semiconductors. The alignment and figure testing of systems with large numbers of elements or off-axis and aspheric elements is a difficult process, and improvements to present techniques are needed. This work describes computer-aided processes of simultaneous alignment and figure testing which can be applied to almost any optical system including these special cases of considerable interest.

1.2 Introduction

The goal of alignment and testing of the components of an optical system is to make the system perform according to its design specifications. Reasons the system does not meet the specifications can include errors in alignment and/or manufacture. The goal of optical testing is to determine the presence and values of these errors. The processes of aberration measurement and reverse optimization described here include attempts to combine individual element quality testing with alignment of these elements. It is especially useful in a system without rotational symmetry that is therefore difficult to align and with components which are difficult and expensive to test when not mounted in the system.

Most optical systems provide an approximately unaberrated, converging or collimated, on-axis output wavefront. It is rare to find a system, unless it is a sub-system, which is

designed to produce an aberrated wavefront. In this sense, a complete optical system containing aspheric elements can be described as "self nulling", because the other elements in the system act as nulling elements for the one under test. End-to-end optical system aberration measurements make use of this property of systems to provide surface figure information without the use of extra nulling components in the testing process.

Reverse optimization¹ is the process of matching the performance of a model system to that of a system under test. If the performance data correspond to an unique set of misalignments of the components, then the model system will have the same misalignments as the system under test. The misalignments of the system under test are then corrected according to the misalignment values of the model. The performance data could be wavefront, ray aberrations or other data which would provide targets for the optimization process. Tilts, decenters, and thicknesses of the model elements are used as variables. The title "reverse optimization" arises because a standard lens design code is normally used to improve the performance of a model, rather than making it worse.

If sufficient sampling of the pupil can be made, the figure of a system element can be determined with an end-to-end test. This eliminates many of the difficulties of testing components of the system, thereby providing a less expensive alternative to conventional alignment and figure testing, or a supplement to methods already used.

1.3 Past and Related Works

The literature contains several works on the concept of computer aided alignment of systems. The process began with the use of computers in wavefront analysis and design tolerancing. Programs such as FRINGE² and WISP³ allowed computer analysis of aberrations, useful in determining misalignments. Computer modelling allowed for easy determination of change tables and therefore the dependence of aberrations on manufacturing parameters.

Thompson's⁴ work on wavefront aberrations of systems suggests ways to align a system from wavefront data, but not an analytic solution to the alignment problem. He remarks that it is possible to confuse various forms of astigmatism arising from design and misalignments. It is only when a least squares iterative solution to the simultaneous differential equations arising from the alignment change table is used that an alignment solution is possible, unless the system in question is trivial.

Lawrence and Chow⁵ showed that it is possible by use of multiple fields and segments of the pupil to separate aberrations due to component misalignments from the nominal aberrations produced by the aligned system, and to recognize surface defects in individual elements. But, since the matrices describing the alignment problem do not lend themselves to a useful analytical solution, Jeong, Lawrence, and Nahm¹ used the least squares iterative process present in optical design codes to solve the differential equations numerically, separating optical surface misalignments from ray aberration data.

Figoski et al⁶ demonstrated the usefulness of this approach in an alignment of a three-mirror telescope. They used CodeV ALI⁷ software, a program design to optimize the

performance of a misaligned system. Their project required extensive figure testing and limited variable use in the alignment process.

Jeong and Lawrence⁸ extended their process of reverse optimization to detect limited defects in one surface figure of a three mirror system, modelling the surface as a grid of spline terms. They demonstrated in simulation that the optimization could be done.

Wong⁹ suggested the use of a Zernike frequency filtering method in removing alignment induced wavefront errors from interferometric tests of surface figures.

1.4 Organization of Dissertation

Chapter 2 describes the equipment designed and constructed to demonstrate the workability of the ray-aberration-based, reverse optimization process of Jeong, Lawrence, and Nahm¹. This system was built to measure longitudinal and transverse ray aberrations of a three-mirror telescope. The results showed that the method of alignment was valid, but also served to point out the shortcomings in a ray based approach.

Chapter 3 discusses wavefront-based reverse optimization and compares the experimental difficulties involved in both wavefront aberration and ray aberration methods of reverse optimization. The wavefront method gives finer spatial sampling and is more appropriate to systems where figure measurement is desired.

Chapters 4 describes simulations done using the wavefront aberration technique to align a Cassegrainian telescope in simulation.

Chapters 5 and 6 describe tests that include figure data from multiple arbitrarily deformed surfaces in simulations with a Cooke triplet and two-Petzval System.

Chapter 7 discusses the effects of gaussian noise present in the wavefront data on optimization and alignment processes.

Chapter 8 is a report on experiments with the two-Petzval, OPTECAL¹⁰ telescope to demonstrate that the wavefront aberration technique works.

CHAPTER 2

RAY ABERRATION METHOD

2.1 Introduction

The reverse optimization process was used by Jeong et al^{1,8} to simulate and predict results for a ray-aberration-based, computer-aided alignment procedure for a three-mirror telescope designed by Rockwell International Corp. The following is the description of the construction and testing of a system designed and used to verify these simulations.

The goal was to develop a test system which would gather sufficiently accurate ray aberration data to align a three-mirror, off-axis telescope by means of reverse optimization. The aberration data was to be measured in several field and focal positions required to perform reverse optimization.^{1,5} Criteria for this system included approximately one micrometer measurement accuracy in the measurement of transverse ray position with respect to a central reference ray. Accurate measure of component position on the testbed, specified by the system design tolerances, and accurate performance measurement of the aligned system were also necessary. Another specification was that the input beam be minimally obscured to also allow interferometric measurements for system performance evaluation.

2.2 Physical Layout

The basic method of measurement was a Hartmann test¹¹. The requirements for the test were a light source, a Hartmann screen, the system under test, and a measurement device: film, a human eye, a CCD or a position sensing detector. The equipment constructed for this experiment consisted of a collimated, laser light source, the Hartmann test screen, space for the system under test, and the lateral effect photodiodes (or interferometer). The physical layout is shown in figure 2.1.

The three-mirror telescope was an $f/1.91$ focal system designed and built for Rockwell International Corp. The primary and tertiary mirrors were segments of one large asphere. Separating these mirrors in the design made the system easier to handle and cut, and reduced the weight of the system. It also allowed motion of the tertiary to achieve better imaging. The system had $1^\circ \alpha$ (around the x-axis) and $11^\circ \beta$ (around the y-axis) full fields-of-view.

The components of the three-mirror system were installed on mounts with 6° of freedom each. The three-mirror system was designed to be diffraction limited at $10.6 \mu\text{m}$, or about 17 times the diffraction limit in the visible. Simulations and experiments showed that this system was alignable with the ray-based approach¹. But, a system with such poor nominal performance at the test wavelength did not have well defined alignment states. Many different possible misalignments would achieve the same performance levels without being in the same alignment state.

The light source was a 7 mW HeNe laser. The visible wavelength was desirable to limit the diffraction spot size, thereby allowing small Hartmann holes. Position sensing detectors are also not readily available at long wavelengths. The power level was chosen because it provided an adequate $4 \mu\text{A}$ response from the detector. The maximum input to the lockin amplifier was 5 V, which meant a maximum 10^6 V/A conversion by the transimpedance amplifiers. Another consideration for the laser power was the desire to use a WYKO LaDiTe¹² as a test device at the output of the telescope.

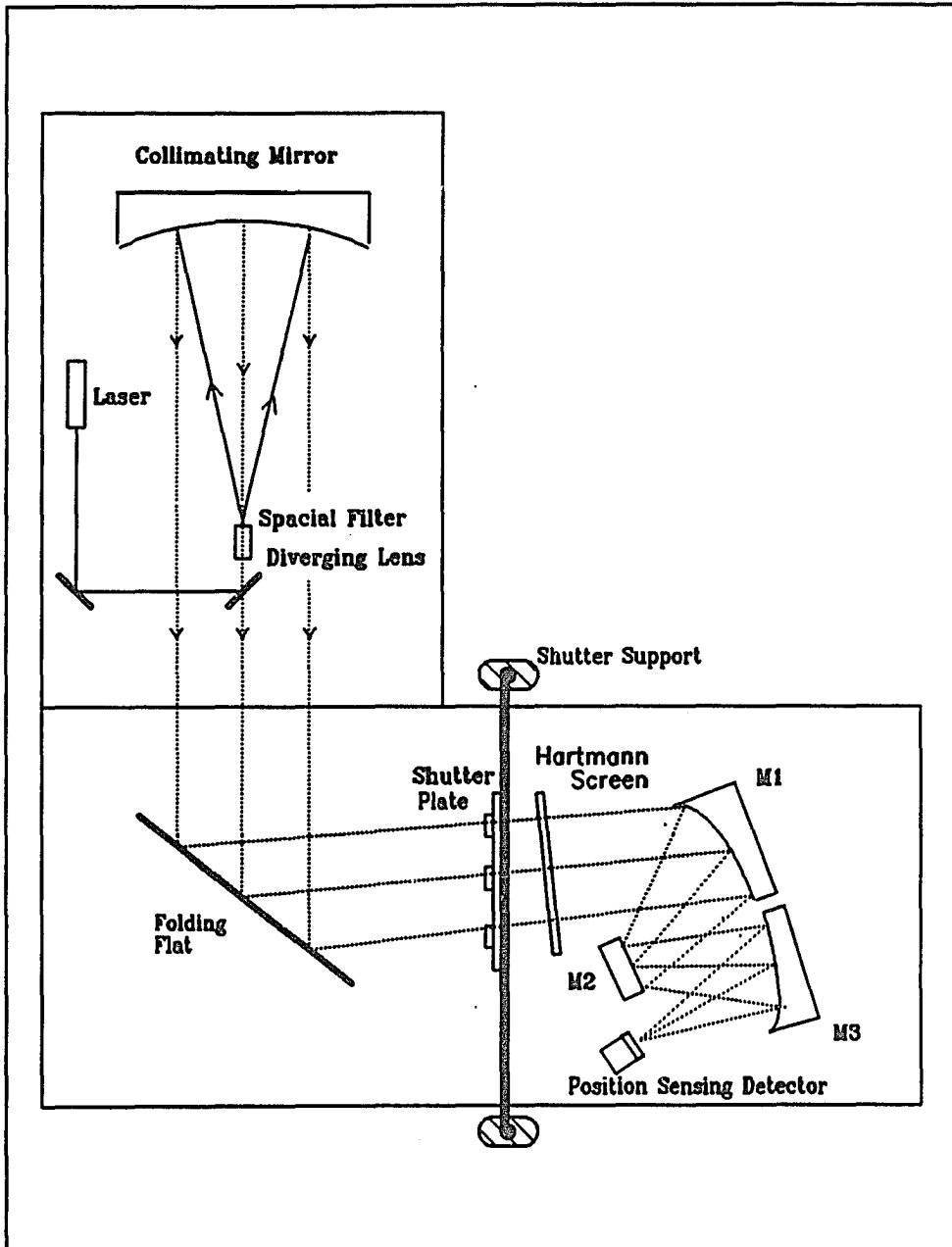


Figure 2.1. Three-mirror test-bench with collimated light-source, Hartmann screen and suspended shutter-plate.

The laser was chopped at 100 Hz, the maximum frequency that resulted in no observable waveform distortion through the system electronics. The modulated source was chosen to allow the system to function in the presence of room light, and to remove the effects of possible constant biases in the detectors.

An $f/2$ diverging lens with a $4\mu\text{m}$ diameter pinhole spatial filter at its focus and a 55 cm diameter, quarter-wave peak-to-valley quality (at $0.63\ \mu\text{m}$), $f/2$ recollimating mirror formed a beam expander. At $f/2$ the diffraction spot size is approximately $4\ \mu\text{m}$. The collimated beam overfilled the system under test which had a 35 cm by 25 cm aperture. The input beam did not have to be collimated for this test. Although the original system design specified infinite conjugates, a diverging or converging beam could have been modelled by the computer. However, the telescope's effective focal length of 78 cm made the use of finite conjugates impractical.

Multiple field points for the system were created by reflecting the beam from a quarter-wave quality peak-to-valley (at $0.63\ \mu\text{m}$), 60 cm square flat which could be rotated about vertical and horizontal axis, thus creating an effective entrance pupil at the location of the Hartmann screen as shown in figure 2.2. The fixed screen position determines the x-y position of the reference, chief, ray. Although this location of the screen was not the designed entrance pupil of the telescope, it was modelled as such to simplify the optical layout. Moving the pupil changed the nominal aberrations of the system, but the model accounted for this.

Five test rays were chosen as being slightly more than the number necessary to supply enough targets for the optimization as shown by simulation^{1,8}. Five rays, one at the center

of the other four, provided a symmetric sampling. A non-symmetric set of rays could have been used, but would have raised the question of bias in the realignment. A minimum number of rays was desired in order to speed up the measurement process and to avoid slowing the optimization with unnecessary target data. Chapter 7 discusses a drawback to this minimalist philosophy. The holes in the Hartmann screen provided four data rays, and a central, reference or chief ray. Three measurement fields provided twelve independent rays. Each ray supplied four pieces of data, x- and y-angles and intercepts. The result was 48 targets. In theory there could be one target per alignment variable¹. The holes were positioned at the greatest unvignetted radii, to give the largest aberrations, hence the most sensitive measurements. The fields were chosen as extremes for the same reason, the larger the aberrations, the more precisely they could be measured as the detector resolution was a fixed and not a proportional value.

The Hartmann hole diameter had to produce a small diffraction spot size for accurate position measurement and yet approximate the transmitted beam as a ray. The 2.5 cm aperture results from the equation derived by Jeong et al¹ to minimize the gaussian beam diameter at the extreme focus positions and therefore the angular measurement error: $H^2 = (L D f) / (1.22 S_0)$ where H is the hole diameter, L is the wavelength, D is the entrance pupil diameter, f is the system focal length, and S_0 is the detector width. In the actual experiments both 2.5 cm and 1.25 cm holes were used with no noticeable difference.

As the rays from different pupil locations could not be distinguished in the focal plane, it was necessary to measure only one ray position at a time. To do this, electronic shutters with diameter larger than 2.5 cm were placed just before the Hartmann screen. These could be operated manually or by the data collecting microcomputer. The shutters were

supported by a rod over the table surface attached to the floor, in order to isolated vibrations from the opening and closing of the shutters from the table.

The positions of the five output spots for each focus and field were measured using a UDT PIN/4D lateral-effect photodiode with a 2.5 x 2.5 mm active surface, figure 2.3. This detector was chosen for its small surface area. Precision of position measurement is inversely proportional to surface area.¹³ A 6.3 cm² detector was also available for a larger capture range if necessary. An ideal accuracy of spot position measurement was shown in simulation to be 1 μm, the theoretical resolution limit of this type of detector⁸. Repeated measurements of a stationary spot showed that the repeatability was 3 μm. Further simulations showed this value to be allowable. The effects of noise on optimization are discussed in chapter 7. There was a long-term drift of the system, not noticeable in the original noise measurements. This limited the amount of data that could be taken and raised the overall noise level. The listed precision of the micrometer that controlled focus was 0.01 mm direct read and 0.001 mm with the vernier. At f/2, and with 10 mm between the extreme foci, an error of 0.01 mm in defocus represented a transverse ray error of 1.3 μm, significantly less than the 3 μm detector error.

The output current of one data lead, the +x lead for example, was an exponential function of the distance of average center of energy of the spot from the +x anode. If the center of the device was defined as x=0, the distance of the spot from the +x contact would be $d=L/2 - x$, where L was the width of the device in the x direction. The photocurrent would then be $I = I_0 e^{-Ad}$ where A was characteristic of the device material and geometry, and spot size and intensity¹³. The position reading in a fast system may be distorted because the spot size at the detector may change a great deal with focus. The equation for the -x

component was similar. The quantity $I(+x) - I(-x)$ was therefore proportional to $\sinh(Ax)$. Having made the approximation that A was small, $\sinh(Ax) \approx Ax$ and x was given by $[I(+x) - I(-x)] / [I(+x) + I(-x)]$. This approximation is the form that was used.

The x returned by the above equation was dimensionless. It represented a fraction of the detector surface. If the device behaved ideally, the real position, X , would be the dimensionless x multiplied by one half the detector width. It was necessary to find the calibration factor by experimental means because the devices do not behave ideally.

The detector was mounted on a micrometer-driven translation plate and one of the output spots was focused on the detector. An output spot was used in order to have similar intensity as during the alignment tests. The real X and dimensionless x were then recorded and a linear regression performed. The data reduction program calculated the X 's by multiplying the dimensionless output by the slope found in the regression. The constant for Y was calculated separately because the devices are not symmetrical. The final operating program contained a detector calibration routine.

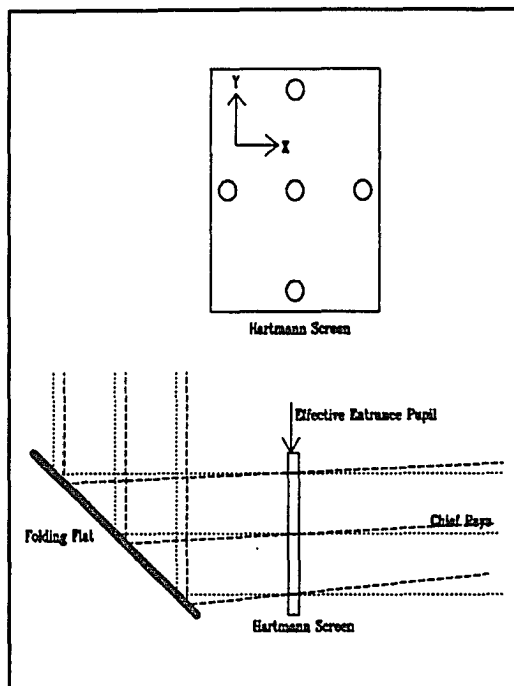


Figure 2.2. The Hartmann screen defines the chief-rays and is therefore located at the entrance pupil.

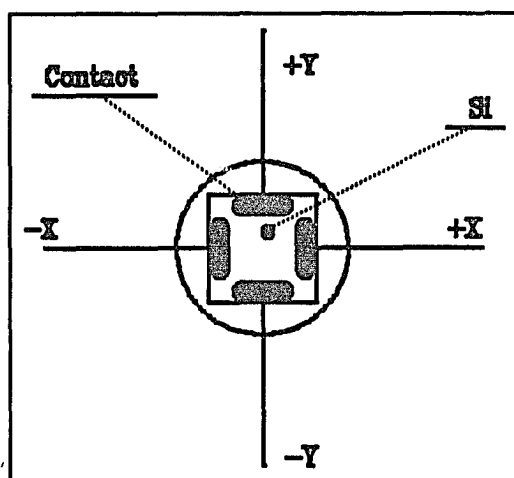


Figure 2.3. Position sensing detector.

2.3 Experimental Operation

A microcomputer was used to run the experiment and take data. A schematic diagram of the data taking system is shown in figure 2.4. The operator would set the desired field position by adjusting the folding flat. The detector was then placed in the correct focal position with the reference ray centered on it. The computer ran the following sequence: selecting a shutter, selecting the detector lead, and reading the lockin amplifier through an RS-232 connection. After this sequence, the next detector lead was selected and the lockin read again. After all four

leads were read a new ray was selected with the electronic shutters, and the measurement sequence repeated. The cycle of five shutters (five rays) was repeated 20 times to allow high frequency noise, mainly electronic and

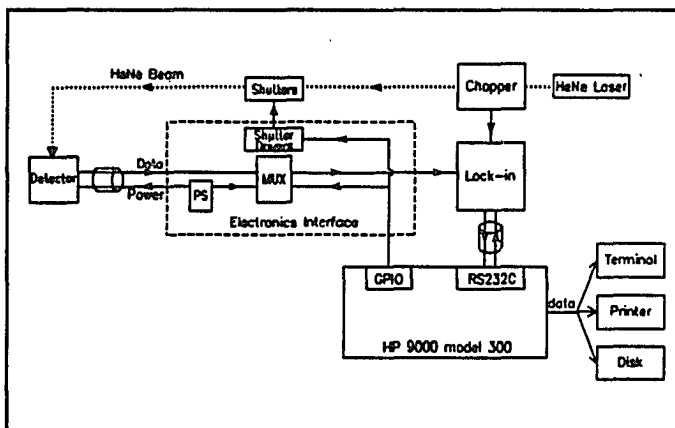


Figure 2.4. Operating system schematic.

vibration, to be averaged out. Various lead-reading patterns were tried, to remove the effects of drift. After this cycle, lasting about 12 minutes for 400 measurements, the operator would move the focus and/or field position. One run, a complete iteration, required approximately 2.5 hrs for 3600 total measurements.

At the completion of a run, the computer would calculate ray angles and intercepts from the data, and output them in a form suitable for input into AccosV¹⁴. This was done on hard copy and input by hand, though modem or disk input would also be possible (and

desirable in cases of many targets). It would also be possible to use a microcomputer that included optimization and modelling software to run the entire experiment, thus generating misalignment data immediately.

The target data was loaded into AccosV¹⁴ and the reverse optimization process was applied. The three-mirror system was adjusted according to the results of the reverse optimization. The measurement and optimization process was repeated and iterations continued until the adjustments were too small to make or the performance would no longer improve.

2.4 Experiments

Preliminary experiments were conducted with a two-mirror, Dall-Kirkham system to "shake-down" the test equipment. The results showed that the system was working. Unfortunately time-budgeting and the poor quality of the telescope optics did not allow for a thorough study with this simple system.

The three-mirror system was aligned by conventional means. The components were set in rough alignment on the optical table as determined by the global coordinate model of the system, then adjusted to make the best, smallest, Hartmann pattern distinguishable by the naked eye. It was not possible to use the interferometer to help with the initial alignment as there was too much aberration in the output beam to form a readable interferogram. We then started the computer aided alignment procedure.

The first attempt at optimization utilized all 12 tilt and decenter variables of the three mirrors. This proved impractical as the design tolerances on the decenters were too large to

include them as optimization variables. Including these variables, especially those of the secondary mirror, caused the solution to oscillate. Even though the mirrors move independently and are modelled as such, there is some coupling in the different degrees of freedom in the mirror adjustment during optimization. If the model adjusts one element by a very large amount, the errors in the one element effectively drown out the other variables. The main factor in this effect is noise in the data taking, but even with perfect data, the least squares optimization does not arrive at a perfect solution in a finite number of iterations due to computer roundoff-error and finite solution space. We reduced the number of variables used in the reverse optimization to include only the most sensitive to misalignment and began the realignment process again.

The system was aligned using only four degrees of freedom, the four tilts of the primary and tertiary mirrors. The design tolerances on these four tilts were $0.3 \mu\text{r}$ as opposed to $1.5 \mu\text{r}$ for the secondary mirror tilts. The design tolerances on x and y decenters of the mirrors were 0.25 cm, which we assumed were met during the manual alignment. The secondary was allowed to move in one intermediate iteration, the fourth, which corrected a visible tilt in the alpha (around the direction of decentration) angle. There were six total iterations. Figure 2.5 shows the corrections made to the mirrors vs. iteration and figure 2.6 shows calculated 80% RMS spot size vs. iteration. A damped oscillation can be seen in both. Ideally the

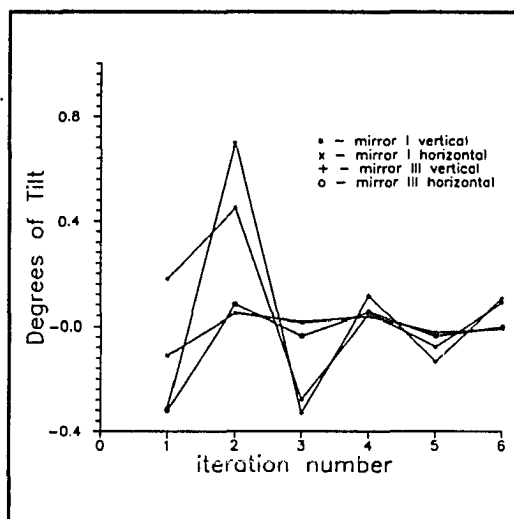


Figure 2.5. Mirror adjustments during alignment.

alignment should converge in only one iteration, but noise in the data and mismodelling made more necessary.

The results after this first run were spot sizes of 87 μm , 98 μm , and 139 μm . for the central, extreme sagittal and extreme tangential fields, as calculated by AccosV¹⁴ where the design spot size was 100 μm in each field. The actual spot size turned out to be a factor of 3 larger than the spot size calculated from the Hartmann test data. This discrepancy indicates a modeling and/or sampling problem which is discussed in Results. The spot size increased slightly on the sixth iteration, indicating the system was in oscillation. The alignment reached the state where no further improvement in performance was possible and experimental error produced a slightly different set of targets for each optimization, causing the oscillation.

The aligned system was perturbed to see if the alignment procedure would bring it back to a comparable, similar performance level, if not the same configuration. A blind change was made to six of the tilt micrometers. The first measure of the new system showed it to have changed performance from an average calculated spot size of 100 μm to approximately 350 μm .

A set of four iterations brought the system back to alignment. There were differences in this configuration compared to the previous solution that were larger than could be accounted for with micrometer error, which indicated that there were several configurations of misalignment with the same performance levels, a solution space, rather than a single solution to system misalignment.

After the initial trials, the test setup was adjusted to accommodate interferometric

testing of the telescope. The $f/2$ lens that focused a spot on the pinhole spatial filter was replaced with a beam expander and a microscope objective and the $4\mu\text{m}$ pinhole was replaced with an $8\mu\text{m}$ pinhole to increase the intensity of the test beam. To compensate for the higher test beam intensity, the hole diameters were reduced to 1.25 cm . There was a large tolerance on hole size, and this change did not reduce the accuracy of the alignment tests.

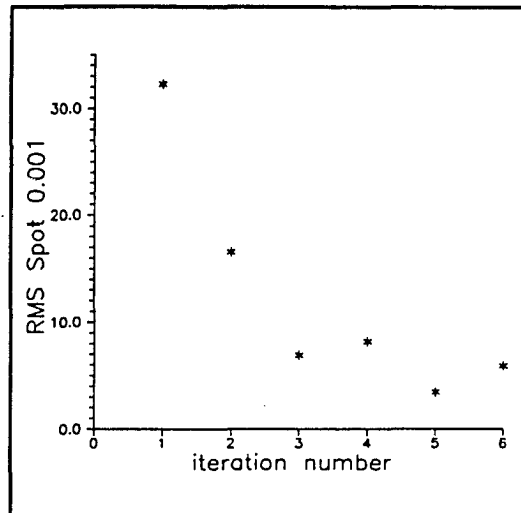


Figure 2.6. Alignment improvement vs. iteration.

The electronics of the transimpedance amplifiers were improved to eliminate a large electronic phase shift error. As the spot positions were measured in three foci, we had redundant data (as it takes only two points to define a line) and therefore had a check on the measured collinearity of the rays. The two extreme foci are used for data, and the third, best focus, data point as the check. Data points that had large collinearity errors could be weighted or left out of the optimization. Before the correction to the electronics, errors in spot position based on the collinearity of up to $20\mu\text{m}$ were not unusual, whereas the precision for a single spot position measurement was about $3\mu\text{m}$. We had blamed this on nonlinearity in the photodiode. After the electronic corrections, these errors fell to the order of the precision of the spot positions, $3\mu\text{m}$, which is the measurement expected. As the error is the same as that of spot position, we concluded that the effects of gaussian beam shape and diffraction due to the Hartmann holes are negligible compared to our other errors.

The decrease in data noise allowed the alignment process to take only about three iterations instead of six as in the first run. But, the actual improvement in performance due to realignment accuracy of alignment did not appreciably change.

2.5 Results

The computer-aided alignment produced convergence in the three-mirror system's alignment. The system could be aligned with the method, then perturbed, and the alignment procedure would return the system to a very similar state. Convergence took three to five iterations and could be done in one or two days. But, the final alignment of this system was approximately a factor of three larger than the ideal 100 μm spot size. The rays, as measured by the test, were those corresponding to the almost ideal aligned system as modelled in AccosV¹⁴ but the system did not perform as well as predicted. Among the problems that could have been responsible for this disagreement were errors in the figure of the real mirrors, the modelling, sampling, or in the wavefront of the input beam.

The most likely source of the unsatisfactory spot size were errors in the actual figure of the mirrors. Because of their aspherical figure, the mirrors could not be tested by interferometry without nulling. The equipment was unavailable to the mirror manufacturer. The mirrors were measured only by profilometry. If there was an error in the mirror figure(s) it would have had the same result as if there was an initial modelling error, a convergence to a non-ideal state, which is what was observed. Chapter 4 discusses results of mismodelling systems.

The AccosV¹⁴ program interpreted the "aligned" Hartmann data as indicating a better performance of the system than actually existed. This indicates a sampling problem. An error

in modelling alone would result in faulty alignments, but the Hartmann data would indicate the large spot size and the optimization would not converge well. As the Hartmann holes only sample one zone of the mirror, an aspheric shape error would not be detected by this test. However, in only the presence of under-sampling alone, not enough targets, where the angles and intercepts of the 15 rays could correspond to more than one alignment state of system perturbing the system could result in reconvergence to a different state, which was not the case. The effects of sampling in terms of noise are discussed in Chapter 7.

Input beam aberration was also investigated as a source of error. Interferometry performed on the input beam with a Shack cube showed that there were two or less waves of aberration across the center 40 cm of the pupil. There was some slightly larger error around the central hole of the collimating mirror, but that is to be expected due to material stress. The small magnitude of input beam aberration could not account for the large observed spot size. The reverse optimization method could have corrected the system for small amounts of input beam aberration assuming that misalignments of the telescope could compensate for errors in the input system.

2.6 Conclusion

The work with the three-mirror system showed that reverse optimization was a viable tool for system alignment as the system performance improved over the alignment by hand and the alignment iterations produced a converging set of corrections rather than being trapped in local minima.

The chief advantage of the Hartmann test is large capture range. It is a direct ray trace and removes worry about the relatively delicate alignment of an interferometer, and can be used with rough surfaces. Another advantage is that rough visual alignment is simplified by having the Hartmann screen available for use.

A measurement accuracy of about $1\ \mu\text{m}$ of a light spot is not easy to accomplish. Detectors for IR wavelengths are not readily available or easy to use. Also, it is difficult to digitize Hartmann data for a reliable computer analysis of system aberrations through a program like FRINGE². Limited sampling over the pupil can also give unreliable performance analysis. The number of rays required for figure measurement make data acquisition time unreasonably long. The difficulty in obtaining data for just the misalignments (only fifteen Hartmann rays) also shows the desirability for an easier measurement system like the wavefront method.

An unforeseen problem with this test was the large optical system aberrations at visible wavelengths. As some measurement noise increases with signal, the noise due to the large nominal aberration was much larger than it would be in a diffraction limited system.

The Hartmann system is a practical, low-cost test system for alignment of optics, but the setup used lacked accuracy due to slow drift, and the time of measurement was proportional to the number of rays used. Other ray-based measurements such as Ronchi rulings may provide better ray-aberration data. UDT has lately come out with a more accurate version of the lateral effect photodiodes, and that might improve the performance of this type of system. Also, some type of frequency coding of the Hartmann rays would allow simultaneous measurements of the spot positions at the focal plane, eliminating some drift problems.

CHAPTER 3

INTRODUCTION TO WAVEFRONT MEASUREMENT IN REVERSE OPTIMIZATION

3.1 Problems with the Ray Aberration Approach

The lack of data on the exact surface figures of the components in the three-mirror, ray-aberration experiment described in Chapter 2 made evaluation of the procedure difficult. Figoski, Shrode and Moore⁶ performed an interferometric alignment of a similar system using the ALI feature of CodeV⁷, in several stages and after extensive component testing. Methods of modelling and reverse optimization require a precise knowledge of the system under test, or compensation for lack of figure data. For a system with asymmetric or highly aspheric elements, the nulling and interferometric testing could be a costly and time consuming process. Misalignment of test components is a problem addressed by Wong⁹, who used a computer modelling and Zernike filtering system to compensate for alignment errors in test components. The best solution would be a testing method which could align components without extensive testing and supply information on individual element surface figures.

A simulation of simultaneous component alignment and figure determination of one surface of a three-mirror system using a Hartmann test was described by Jeong and Lawrence⁸. This method relied on the precise measurement of ray intercepts and angles produced by a Hartmann pattern, then a reverse optimization of an ideal system to match the misaligned system. Lawrence and Chow⁵ investigated the possibility of analytically separating aberration effects from figure errors, but in the case of most optical systems it is necessary to apply numerical methods such as the least squares fit of reverse optimization.

There are certain inherent difficulties in the Hartmann type test in computer-aided alignment: the number of measurements required, the time to take these measurements, and the measurement accuracy. The Hartmann measurement process for 3 fields of 5 rays each took approximately 3 hrs, but further automation and reduction of noise would have lowered this time. This was a total of 15 rays (each measured 20 times and averaged). The ray-set required for figure determination of one surface was 55 rays⁸, a factor of 4 larger than our former Hartmann test requirements, or a projected measurement time of 12 hrs for the test setup that we used. For a fill factor of one in a square grid of 2.5 cm holes, the maximum number of holes that fit in the 35 cm by 25 cm aperture, not including vignetting, is thirty-five. If the figures of the other two surfaces were modelled or more surfaces were involved, the Hartmann system would become unmanageable as the system was subject to drift during measurement. Constant comparison between reference- and test- ray such as an electronic bridge arrangement may have helped this problem.

3.2 Wavefront Method

In order to determine surface figures of components, it is necessary to have a higher spatial frequency sampling of the system wavefront than in the case of misalignments. In the case of parametric equations of the component surfaces, at least as many zones of the elements need to be sampled as there are terms to the

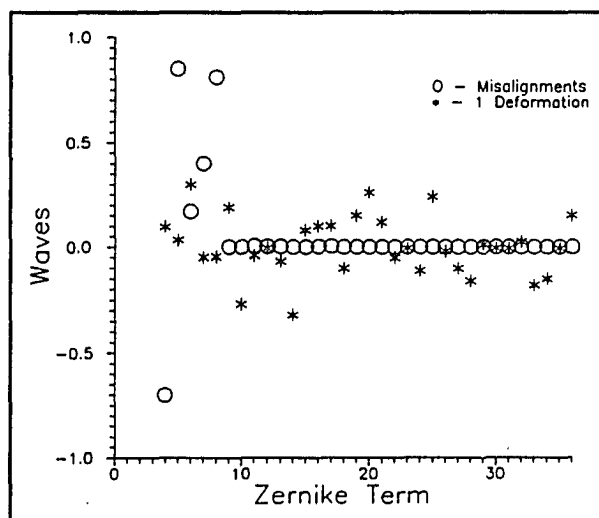


Figure 3.1. Zernike coefficients for misalignments and deformations.

equation. The determination of an asymmetric surface figure error obeys the Nyquist sampling theorem. A sampling rate less than twice the frequency of the deformation results in aliasing.

The Zernike coefficients describing the wavefront of a two-Petzval optical system are shown in figure 3.1. In one case there are misaligned elements in the system, and in the other, the system has one element with a deformation. The misalignments and the figure deformation used for this figure were selected to have nearly equal RMS wavefront error. The Zernike polynomials are orthogonal and complete on a unit circle. Because the polynomials contain powers of trigonometric terms, they can be considered to represent increasing spatial frequency with increasing order. Figure deformations that result in wavefront aberration of high frequency can therefore be partially separated from the effects of misalignments. To remove the effects of high frequency surface errors, a good first approximation would be to decompose the output wavefront of a system into Zernikes and set the terms above Zernike 10 to zero, the equivalent of a low-pass filter. Figure 3.1 can be viewed as a frequency spectrum of the convolution of misalignment or deformation wavefronts with the nominal system OTF. The deformation possesses non-zero low order terms. As the effective wavefront aberration due to the deformation approaches a delta function, its spectrum should approach a constant term.

It is possible to create a low frequency deformation which looks like an alignment error. It is therefore necessary to place constraints on the surface variables used in the reverse optimization process. Jeong and Lawrence⁸ solved this problem by constraining three points on a surface to zero height, defining a plane of the surface.

3.3 Comparison to Hartmann Test

The description of aberrations as OPD or rays is equivalent for optimization. There is no mathematical advantage to using OPD's. If the wavefront is known to the desired accuracy, all data provided by the ray type test can be derived. The same is true of a ray aberration test with fine enough sampling. The wavefront could be reconstructed and used for optimization.

Using OPD, interferometer measurements, instead of ray measurements, solves many of the problems associated with the Hartmann test. Using OPD measurements, the elements' surface figures can be optimized along with the misalignments because of the higher spatial sampling rate. The alignment aberrations are typically low order, while irregular figure errors produce higher orders of aberration. The higher the spatial sampling rate, the finer the surface detail that can be measured. The spatial sampling rate in the OPD method is not limited by diffraction due to sample size. There is an optimum Hartmann hole size described in Chapter 2. By using, for example, a 100 x 100 pixel CCD to sample the exit pupil, we get an effective 10,000 hole Hartmann screen, which would be impossible to use due to diffraction. The OPD method can be thought of as a Hartmann test with an extremely large number of rays, but virtually no increase in experiment time for an increase in ray number. The Hartmann system averages the aberration over the area sampled by the finite-sized rays. The OPD method's higher frequency spatial sampling rate reduces the problems of aliasing.

The Hartmann system has advantages such as capture range and nominal aberration tolerance. The interferometers are limited in the amount of aberration they can process. For a Mach-Zehnder, there has to be a small enough spot to get enough energy through the spatial

filter to be able to make a reference beam, and for phase shifting or shearing interferometers there are 2π phase problems for large aberration. The Hartmann test also has a more simple optical setup because interferometers are more sensitive to their own misalignment than Hartmann detectors. The Hartmann detectors and electronics for our three-mirror experiment were significantly less expensive than a typical phase shifting interferometer.

3.4 Conclusion

Assuming near-visible diffraction limited optical systems with good scatter performance and good initial alignment state, the OPD system of measurement has the advantage over the Hartmann type of measurements. The practical spatial sampling rate of the OPD system is higher than that of the Hartmann test, and the data is easier to process digitally.

The cases where the Hartmann test or other non-interferometric tests would be most useful are systems that are so misaligned or with such rough surfaces that interferometry is impossible. Another case is where budgetary considerations greatly outweigh accuracy, or where surface figure is well known.

CHAPTER 4

SINGLE MIRROR AND CASSEGRAINIAN TELESCOPE

4.1 Introduction

In preparation for simultaneous realignment and figure testing, the wavefront aberration method was tested on some simple optical systems. The process of reverse optimization had been shown to work with ray aberration data^{1,8}, but it was unknown whether it was practical to use wavefront aberrations which did not contain explicit x- or y- slope data. Each ray traced through the system under test in the ray-based method provided four pieces of data, lateral and angular ray aberrations in x and y, while each point in the wavefront provided one piece of data, the OPD.

The first systems chosen to test the method were a single mirror, and a two mirror system. Both of these systems were simple enough so that the alignment problem could be approached somewhat intuitively. In the case of the single mirror, realignment can be done analytically, without numerical methods.

4.2 Single Mirror

Alignment simulations were performed with a single element to test the OPD method on a simple case. A spherical mirror, evaluated at infinite conjugates, was modelled in Super Oslo¹⁵. The mirror had a 10 cm focal length at $f/5$. The tilts of the mirror in orthogonal directions were used as the alignment variables. Three rays could be traced through the system. One ray was a reference, on the optical axis at $(x/r, y/r) = (0, 0)$ in the pupil. The other two rays were located at $(x/r, y/r) = (.7, .7)$ and $(-.7, -.7)$ in the pupil. The optical path differences between the two rays and the referenced ray were used as the targets for optimization. While the computer treated the OPD targets as rays, it should be noted that the

rays actually determined wavefront OPD at specific coordinates in the pupil.

The mirror was first tilted in the α direction by 0.50° . The OPD of the first ray changed from 0.5 waves to 111.1 waves. The amount of aberration was large because there was no refocusing. The optimization target was $\text{OPD}(\text{ray } 1) = 111.1$ waves. The variable was the tilt of the mirror. The model misaligned to $\alpha = 0.50^\circ$, the same value as the misalignment of the system under test.

At $\alpha = 0.0^\circ$, $d(\text{OPD ray } 1)/d\alpha = 208.2$ (waves/degree). If the mirror had been aligned from just the sensitivity matrix, the resulting α misalignment value would have been 0.53° .

The experiment was repeated with misalignments of $\alpha = 0.5^\circ$ and $\beta = -0.25^\circ$. The OPD of the first ray was measured as 164.8 waves. Using only one target, the system optimized to $\alpha = 0.377^\circ$, $\beta = -0.377^\circ$, an incorrect realignment, but one that matched the OPD of the first ray. The second ray of the system under test had an OPD of -147.5 waves. When the optimization was performed with two targets and the two variables, the model optimized to $\alpha = 0.49^\circ$, $\beta = -0.26^\circ$. The small error in calculated misalignment was due to round-off error in the data. The analytical solution to this case is now of the form:

$$\begin{bmatrix} \frac{\delta OPD1}{\delta \alpha} & \frac{\delta OPD1}{\delta \beta} \\ \frac{\delta OPD2}{\delta \alpha} & \frac{\delta OPD2}{\delta \beta} \end{bmatrix} = \begin{bmatrix} A & B \\ C & D \end{bmatrix} \quad (\alpha=0, \beta=0) \quad (1) \text{ Sensitivity matrix}$$

$$\begin{bmatrix} OPD1 \\ OPD2 \end{bmatrix} = \begin{bmatrix} E \\ F \end{bmatrix} \quad (2) \text{ Constraints}$$

But, the derivatives in the matrix are functions of α and β . As the misalignments move the system farther from the aligned state, the solution departs further from linear. One of the motivations of the damped least squares fit in reverse optimization is to eliminate the many alignment cycles that would be necessary if only linear corrections were made.¹

The single mirror could be realigned with very few targets and only required one field. For the case of a mirror with only one degree of freedom, only one independent ray was required to align it. As degrees of freedom, variables, were added, more targets were required. Jeong et al¹ found a one-to-one correspondence between degrees of freedom and number of targets required and a similar correspondence between number of elements and number of fields required.

4.3 Cassegrainian Telescope

A Cassegrainian telescope, figure 4.1, was modelled in Super Oslo¹⁵ software; its prescription is given in table 4.1. The mirrors had four alignment variables each, two rotational and two decenter. Individual field foci comprised another five variables. The aligned state RMS OPD was 0.1 waves, on-axis. The diffraction MTF on axis can be seen in figure 4.2.

Misalignment tolerances for the system are given in table 4.2. The aberrations due to misalignments are well understood, as described by Thompson⁴. The tolerance for decenter of the primary is extremely large, especially with decentering of the secondary as a compensator. The motion of these two elements together is the same as decentering of the pupil. This could be a critical factor if vignetting were important to performance, but in this case, it was not a concern.

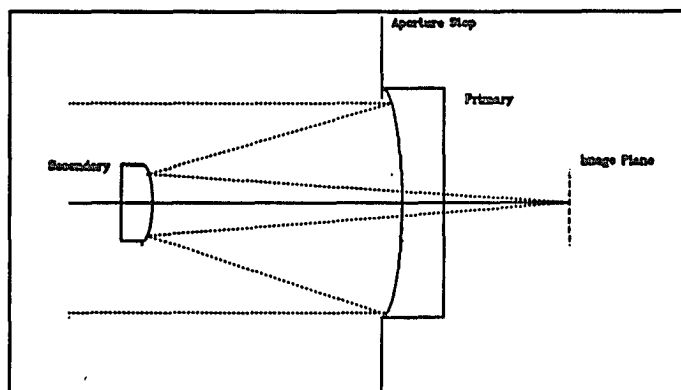


Figure 4.1. Cassegrainian telescope.

Table 4.1. Prescription of Cassegrainian telescope.

Surface	Note	Radius	Thickness	Glass	Conic C.
1	Object		Infinity	Air	
2	Stop		0		
4	Primary	-268 cm	-94 cm	Mirror	-1.00
7	Secondary	-111 cm	146 cm	Mirror	-2.20
9	Image				

Table 4.2. Tolerancing of Cassegrainian telescope.

Surface	Variable	Quality	% Change
3	Tilt	0.15°	65
	Decenter	10.00 mm	47
7	Tilt	0.05°	66
	Decenter	0.75 mm	53

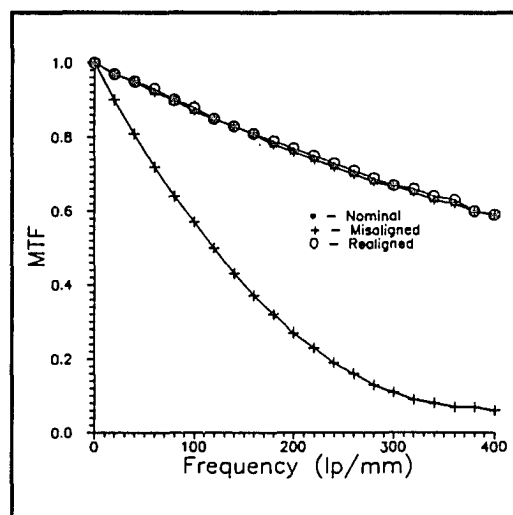


Figure 4.2. MTF's of nominal, misaligned and realigned Cassegrainian telescope.

4.4 Misaligned System

The mirrors were tilted and decentered according to table 4.3 column 3. The five fields, shown in figure 4.3, were independently focussed for minimum RMS spot size as would be done in interferometry. Focus was used as a variable to allow for the refocussing. The resulting on-axis RMS OPD was 1.69 waves at best focus. The resulting MTF is shown in figure 4.2.

Twenty simulated rays, rays 2 - 5 in figure 4.4, were traced through the entrance pupil, four in each field. Multiple fields were used to separate alignments of different elements, similar to the "wavefront tomography" of Lawrence and Chow.⁵ The OPD's for each ray were then recorded. We assumed that any aberrations introduced by the test equipment could be subtracted from the data.

4.5 Realignment

The OPD's were entered as targets for the optimization. The model started with no tilts, decenters, or defocus. The variables were the eight tilts and decenter of the two mirrors, and the five field foci. Table 4.3, column 4 shows the tilt and decenter values of the optimized system. These tilts and decenters of the optimized model system were used as corrections to the misaligned system. The realigned system had an RMS OPD of 0.11 waves and the MTF shown in figure 4.2. The uncorrected decenters of the elements in both x and y are in the same direction. The elements have a small decenter with respect to each other. The telescope performance has a large tolerance for decenter with respect to the pupil, as shown in table 4.2. The residual misalignment does not greatly effect the performance.

Table 4.3. Optimization of Cassegrainian.

Surface	Variable	Misaligned	Optimized	Residual
4	α tilt	0.30°	0.40°	-0.10°
	β tilt	0.50°	0.44°	0.06°
	y decenter	1.3 mm	-6.1 mm	7.4 mm
	x decenter	2.5 mm	9.4 mm	-6.9 mm
7	α tilt	1.00°	0.87°	0.13°
	β tilt	-1.20°	-1.16°	0.04°
	y decenter	6.4 mm	-4.6 mm	10.9 mm
	x decenter	8.9 mm	15.2 mm	-6.3 mm

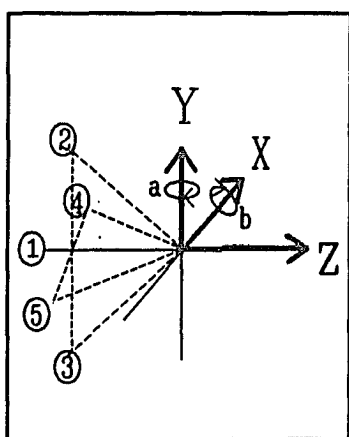


Figure 4.3. Fields and coordinates.

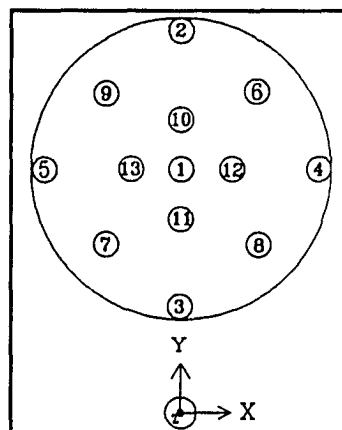


Figure 4.4. Rays used in optimizations.

4.6 Conclusion

The alignment process brought the performance of the Cassegrainian telescope almost identically back to the original level. There were some residual misalignments. These misalignments had a negligible effect on the performance of the system, and are therefore not corrected by the alignment procedure. The decenters of the primary mirror would probably not be used as variables in a normal alignment procedure, as decentering of the pupil does not matter to the performance, and the variables tend to optimize to erroneous values.

The Cassegrainian system had a large amount of nominal wavefront error at fields larger than 1/4 degree full-field. It is difficult to misalign the system enough to give noticeably worse performance at full-field. Near full-field, the misalignment-induced aberrations are difficult to pick out of the nominal. The compensation for this was that residual alignment errors had a negligible effect on the overall performance of the system. If the system had stricter tolerance requirements, the residual misalignments would be correspondingly smaller. The realignment process is performance oriented. The process of reverse optimization and alignment correction will take the system to a state of good performance as measured by the testing used to get data for optimization. This will not necessarily be the designed alignment state.

CHAPTER 5

COOKE TRIPLET

5.1 Introduction

A Cooke triplet¹⁴ was aligned and tested in simulation for figure errors. Changes in performance due to misalignments were easier to detect because the triplet had much better performance than the Cassegrainian telescope. Because the reverse optimization process relies on system performance measurement, the results were more evident with the better optical system.

5.2 Nominal Performance

The Cooke triplet had nominal RMS OPD errors of 0.022 waves on axis, and 0.133 waves at the 1° half-field. The triplet is shown in figure 5.1, and the prescription is given in table 5.1. The diffraction based MTF's are shown in figure 5.2. The tolerances for misalignments are given in table 5.2. The alignment tolerances are given without considering compensation, except for focus. Some misalignments, and curvature errors could compensate each other. If two different alignment states would produce the same performance, the reverse optimization could "choose" either.

The three lenses of the model could be tilted and decentered each in two directions. We allowed five variable field foci for a total of 17° of freedom in the alignment test. The simulated test could use up to 60 rays, in the same ray pattern as the Cassegrainian system.

Table 5.1. Prescription of Cooke triplet.

Surface	Note	Radius	Thickness	Glass
1	Object		Infinity	
4	Lens I	4.3 mm	0.4 mm	SK16
5		-24.8 mm	1.1 mm	Air
7	A Stop			
8	Lens II	-3.82 mm	0.3 mm	F4
9		4.39 mm	1.0 mm	Air
12	Lens III	65.70 mm	0.5 mm	SK16
13		-3.35 mm	8.6 mm	Air
15	Image			

Table 5.2. Cooke triplet tolerances.

Surface	Variable	Quality	% Effect
4	Tilt	0.9°	114
	Decenter	0.05 mm	181
	Radius	20 waves	---
5	Radius	20 waves	---
8	Tilt	0.3°	74
	Decenter	0.01 mm	160
	Radius	5 waves	100
9	Radius	5 waves	64
12	Tilt	0.3°	76
	Decenter	0.02 mm	277
	Radius	20 waves	---
13	Radius	20 waves	42

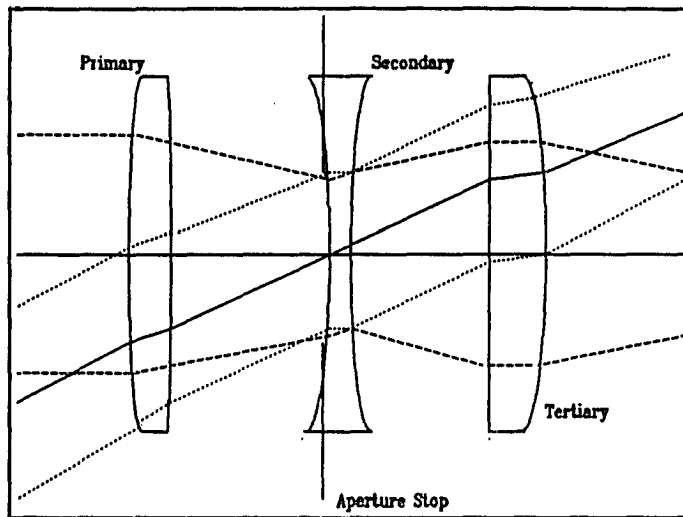


Figure 5.1. Cooke triplet.

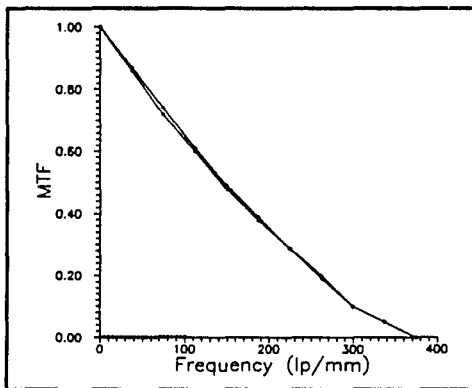


Figure 5.2. Nominal triplet performance.

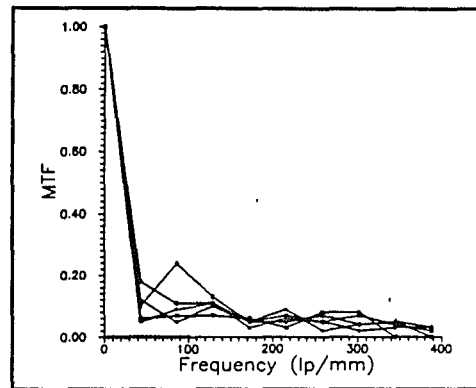


Figure 5.3. Misaligned triplet performance.

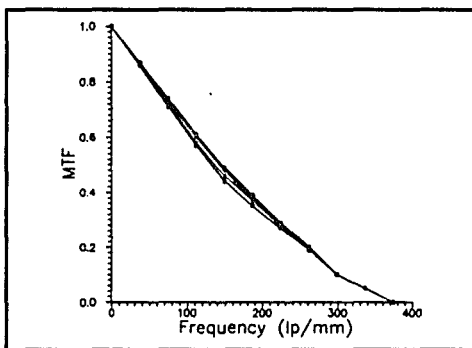


Figure 5.4. Realigned triplet performance.

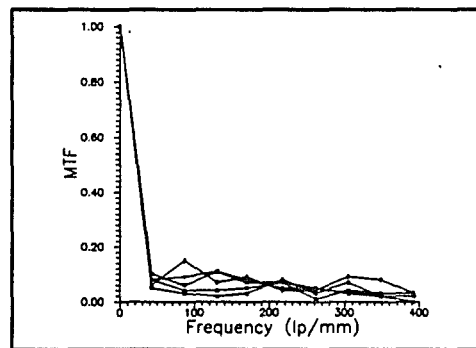


Figure 5.5. Performance of triplet optimized with mismodelling.

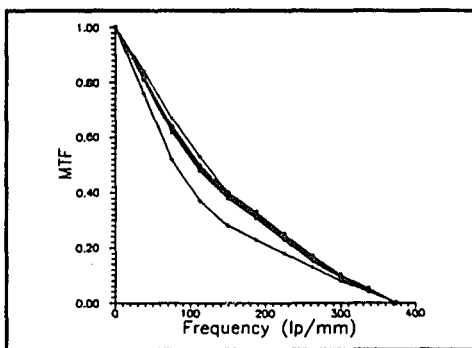


Figure 5.6. Performance of triplet realigned with 6 figure variables.

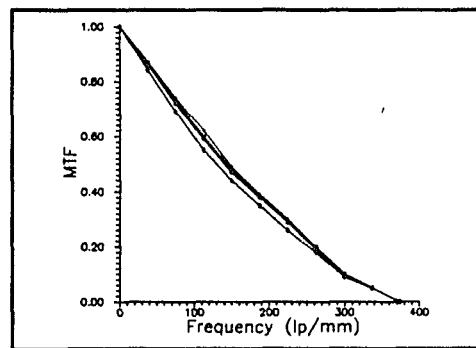


Figure 5.7. Performance of triplet realigned with 4 figure variables.

5.3 Perturbation of Alignment

To test the ability of the reverse optimization process to correct misalignments in the Cooke triplet, a misaligned system was simulated. The model elements were tilted and decentered according to table 5.3, column 3. The resulting RMS OPD errors are given in table 5.4, and the MTF's are shown in figure 5.3. The performance was evaluated in a flat focal plane located at the on-axis best-focus. The misalignments caused a large decrease in performance. The performance data were 60 OPD values, rays 2 through 13 in figure 4.4. The alignment could be done with only twenty rays, but sixty were used to keep the operand (target) number constant throughout the experiments.

5.4 Realignment

The variables for optimization were the 17° of freedom of the system. The operands were the 60 OPD values. The model was optimized with no special damping of variables or weighting of targets. Table 5.3, columns 4 and 5, show the results of aligning the system with the reverse optimization process. The corrected system had RMS OPD's given in table 5.4, and MTF's shown in figure 5.4.

The reverse optimization process with ideal (there was a round-off error of 0.02 waves) data resulted in near perfect realignment of the system. The residual alignment error resulted in a negligible change in system performance.

Table 5.3. Realignment of triplet, misalignments only.

Surface	Variable	Initial	Optimized	Residual
4	α tilt	0.20°	0.11°	0.09°
	β tilt	-0.15°	-0.14°	-0.01°
	y decenter	7.6 mm	7.6 mm	0.0 mm
	x decenter	0.6 mm	0.6 mm	0.0 mm
8	α tilt	0.40°	0.31°	0.09°
	β tilt	0.05°	0.07°	-0.02°
	y decenter	-6.4 mm	-6.4 mm	0.0 mm
	x decenter	2.5 mm	2.5 mm	0.0 mm
12	α tilt	0.30°	0.17°	0.13°
	β tilt	-0.20°	-0.08°	-0.12°
	y decenter	12.7 mm	12.7 mm	0.0 mm
	x decenter	2.8 mm	2.8 mm	0.0 mm

Table 5.4. Performance of realigned triplet, misalignments only.

Field	Aligned RMS OPD	Misaligned RMS OPD	Realigned RMS OPD
On-Axis	0.022 waves	1.250 waves	0.022 waves
+Y	0.044 waves	1.370 waves	0.045 waves
-Y	0.044 waves	1.960 waves	0.043 waves
+X	0.044 waves	1.750 waves	0.047 waves
-X	0.044 waves	1.910 waves	0.041 waves

5.5 Optimization with Modelling Errors

The six surface curvatures of the triplet were altered to simulate an optical system that did not match the model specifications. The new curvatures are given in table 5.5. The aligned performance of the new triplet was comparable to the original triplet.

Target data from the original triplet and the same 17 variables were used for the optimization. Table 5.6 lists the results of the reverse optimization and the resulting residual misalignments. The MTF's of the system are shown in figure 5.5. The optimization did not work, performance was not improved. Because the models of the lenses did not have the correct powers, there was no set of misalignments which could produce a performance equivalent to the system under test.

Table 5.5. Modelling errors in triplet. (* - significant tolerance)

Surface	Nominal Curvature	Modelled Curvature
4	4.30 mm	4.32 mm
5	-24.81 mm	-24.40 mm
8	-3.82 mm	-4.03 mm*
9	4.40 mm	4.41 mm*
12	65.67 mm	98.95 mm
13	-3.35 mm	-3.45 mm*

Table 5.6. Results of reverse optimization with severe modelling errors.

Surface	Variable	Misaligned	Optimized	Residual
4	α tilt	0.20°	2.44°	-2.24°
	β tilt	-0.15°	0.80°	-0.95°
	y decenter	0.30 mm	0.04 mm	0.26 mm
	x decenter	0.20 mm	0.20 mm	0.00 mm
8	α tilt	0.40°	2.51°	-2.11°
	β tilt	0.05°	1.26°	-1.21°
	y decenter	-0.25 mm	-0.30 mm	0.05 mm
	x decenter	0.10 mm	0.13 mm	-0.03 mm
12	α tilt	0.30°	6.05°	-5.75°
	β tilt	-0.20°	1.83°	-2.03°
	y decenter	-0.05 mm	0.11 mm	-0.16 mm
	x decenter	-0.11 mm	-0.14 mm	0.03 mm

Table 5.7. Performance of system optimized with severe modelling errors.

Field	Aligned RMS OPD	Misaligned RMS OPD	Realigned Mismodelled RMS OPD
On-Axis	0.022 waves	1.25 waves	1.27 waves
+Y	0.044 waves	1.37 waves	1.16 waves
-Y	0.044 waves	1.96 waves	1.41 waves
+X	0.044 waves	1.75 waves	1.29 waves
-X	0.044 waves	1.91 waves	1.31 waves

5.6 Optimization with Variable Curvatures

It was possible to correct the problem of uncertain modelling without taking the system apart and testing the lenses individually. The reverse optimization was performed with an additional six variables, the radii of curvature of the six lens surfaces. The original 60 targets were used. The alignment corrections are given in table 5.8. The RMS OPD's of the realigned system are given in table 14, figure 17 shows the resulting MTF's. The realigned performance was not as good as the perfectly modelled system, but it was a great improvement over the previous optimization. Adding curvature as a parameter widened the solution space, and the alignment variables did not get as close to correct as in the perfectly modelled system. There were also some large errors in the measure of the curvatures of the lenses.

Table 5.8. Results of reverse optimization with modelling errors and variable curvatures.

Surface	Variable	Misaligned	Optimized	Residual
4	α tilt	0.20°	0.47°	-0.27°
	β tilt	-0.15°	-0.29°	0.14°
	y decenter	0.30 mm	0.30 mm	0.00 mm
	x decenter	0.20 mm	0.21 mm	-0.01 mm
8	α tilt	0.40°	0.46°	-0.06°
	β tilt	0.05°	0.05°	0.00°
	y decenter	-0.25 mm	-0.25 mm	0.00 mm
	x decenter	0.10 mm	0.10 mm	0.00 mm
12	α tilt	0.30°	0.64°	-0.34°
	β tilt	-0.20°	-0.23°	0.03°
	y decenter	-0.05 mm	-0.04 mm	-0.01 mm
	x decenter	-0.11 mm	-0.09 mm	-0.02 mm

Table 5.9. Performance of system optimized with modelling errors and variable curvatures.

Field	Aligned RMS OPD	Misaligned RMS OPD	Realigned Variable-Curvature RMS OPD
On-Axis	0.022 waves	1.25 waves	0.14 waves
+Y	0.044 waves	1.37 waves	0.11 waves
-Y	0.044 waves	1.96 waves	0.19 waves
+X	0.044 waves	1.75 waves	0.16 waves
-X	0.044 waves	1.91 waves	0.15 waves

Table 5.10. Curvature optimizations, case 1. (* - significant tolerance)

Surface	Nominal Curvature	Modelled Curvature	Optimized Curvature
4	4.30 mm	4.32 mm	4.56 mm
5	-24.81 mm	-24.40 mm	-22.28 mm
8	-3.82 mm	-4.03 mm*	-3.71 mm
9	4.40 mm	4.41 mm*	4.59 mm
12	65.67 mm	98.95 mm	67.58 mm
13	-3.35 mm	-3.45 mm*	-3.30 mm

According to table 5.2, the tolerance table for the Cooke triplet, the curvatures of surfaces 4 and 5 had insignificant effect on system performance compared to 8 and 9, and ,12 and 13. The large tolerance for errors in these two surfaces caused the optimization to wander. The surface changes could be compensated elsewhere in the design.

The simulation was repeated without these two variables. The results of the optimization are shown in tables 5.11-13. The optimization resulted in good analysis of the actual curvatures of the elements and restores performance to almost ideal. The final MTF's are shown in figure 5.7, and were almost identical to those for the perfectly-modelled case.

Table 5.11. Results of reverse optimization with variable curvatures, case 2.

Surface	Variable	Misaligned	Optimized	Residual
4	α tilt	0.20°	0.42°	-0.22°
	β tilt	-0.15°	-0.24°	0.09°
	y decenter	0.30 mm	0.29 mm	0.01 mm
	x decenter	0.20 mm	0.20 mm	0.00 mm
8	α tilt	0.40°	0.54°	-0.14°
	β tilt	0.05°	0.07°	-0.02°
	y decenter	-0.25 mm	-0.25 mm	0.00 mm
	x decenter	0.10 mm	0.10 mm	0.00 mm
12	α tilt	0.30°	0.43°	-0.13°
	β tilt	-0.20°	0.04°	-0.24°
	y decenter	-0.05 mm	-0.05 mm	0.00 mm
	x decenter	-0.11 mm	-0.12 mm	0.01 mm

Table 5.12. Curvature optimizations, case 2. (* - significant tolerance)

Surface	Nominal Curvature	Modelled Curvature	Optimized Curvature
4	4.30 mm	4.32 mm	---
5	-24.81 mm	-24.40 mm	---
8	-3.82 mm	-4.03 mm *	-3.83 mm
9	4.40 mm	4.41 mm *	4.40 mm
12	65.67 mm	98.95 mm	67.18 mm
13	-3.35 mm	-3.45 mm *	-3.36 mm

Table 5.13. Performance of system corrected with modelling errors, case 2.

Field	Aligned RMS OPD	Misaligned RMS OPD	Realigned Variable-Curvatures RMS OPD
On-Axis	0.02 waves	1.25 waves	0.02 waves
+Y	0.04 waves	1.37 waves	0.04 waves
-Y	0.04 waves	1.96 waves	0.05 waves
+X	0.04 waves	1.75 waves	0.04 waves
-X	0.04 waves	1.91 waves	0.06 waves

5.7 Conclusion

The work with the Cooke triplet showed that the process of reverse optimization based on wavefront aberration data could be used to align the elements of a high performance system. It was possible to detect errors in construction and compensate for them, by optimizing the shapes of multiple surfaces and the misalignments of components simultaneously.

We have shown the importance of correct modelling to this computer-aided alignment process. If the system was not modelled correctly, the process failed with severe mismodelling or optimized to less than desired levels.

This series of simulations also demonstrated the effects of compensating variables, as in the case of the large-tolerance curvatures of the system. When variables have large tolerances or pairs of variables compensate well, it was best to either damp one of the pair heavily or leave it out of the optimization entirely.

CHAPTER 6

TWO-PETZVAL TELESCOPE

6.1 Introduction

Alignment and figure testing were simulated for a two-Petzval telescope in preparation for work on the OPTECAL^{10,17} testbed. The model used for the two-Petzval telescope simulations was the model of a system designed for alignment algorithm testing. The experiments done with the two-Petzval model were designed to be repeated with the actual telescope, to test the reverse optimization process. The first experiment corrected misalignments to the elements. The surface deformation experiments were designed to make use of adaptable optics available in the actual two-Petzval system.

6.2 Optical System

The afocal telescope, shown in figure 6.1, was composed of two pairs of achromatic doublets and had 1:1 magnification. The prescription of the system is given in Table 6.1. The optical system was modelled with a perfect, flat wavefront as input. The actual input was a beam collimated by an off-axis parabola. The telescope was afocal, but the system included an imaging off-axis parabola after the last lens. This parabola was modelled as part of the system.

The telescope elements had a total of ten degrees of freedom in alignment, not including focus. The variables were tilts and decenters of the positive elements of each doublet. Two of the alignment variables, x -decenter of Petzval I and y -decenter of Petzval IV, were designed to be used to keep the line-of-sight of the system in line with the interferometers. The x -decenter of Petzval I and the β tilt of Petzval IV compensated so well that one had to be heavily damped or else the optimization would oscillate.

Field position was determined by a flat mirror located at the design entrance pupil. This mirror could be tilted in the x - or y -direction. The fields chosen for the simulation were $\pm 1/2^\circ$ in the y -direction and $\pm 1^\circ$ in the x -direction. These fields were chosen because the exact angles of mirror vs. electronic actuator position were previously determined in testing by Hughes Aircraft Corporation.¹⁸ A folding flat controlled the output beam angle. This mirror was located at a position symmetric to the entrance pupil but not at the exit pupil. This configuration allowed the telescope and interferometer to remain in fixed positions on the bench and kept the interferometer axis aligned with the telescope line of sight. Another approach would be to test the system in double pass, and rotate the entire system under test around its entrance pupil.

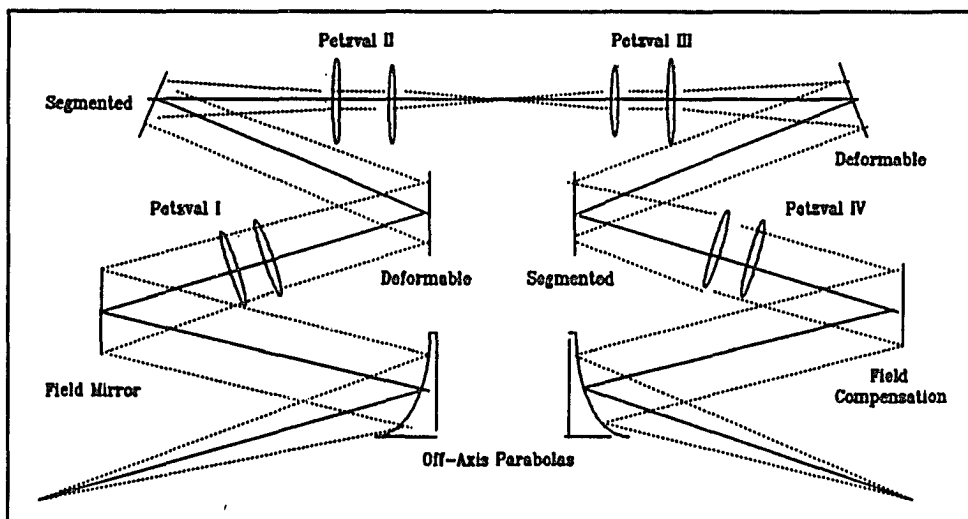


Figure 6.1. Two-Petzval telescope.

Table 6.1. Prescription of two-Petzval telescope.

Surface	Note	Radius	Thickness	Glass	CC
1	Object		-		
2			-12.7 cm	Air	
4	E Pupil			Mirror	
6			52.7 cm	Air	
7	Petzval I	106.2 cm	1.9 cm	FK01	
8		-81.4 cm	6.1 cm	Air	
10	Petzval I	-72.4 cm	1.0 cm	KZFSN4	
11		-509.0 cm		Air	
13			27.0 cm		
15	Deformable			Mirror	
16			-73.3 cm	Air	
18	Segmented			Mirror	
19			34.3 cm	Air	
20	Petzval II	84.4 cm	2.2 cm	FK01	
21		-67.8 cm	9.5 cm	Air	
23	Petzval II	-50.5 cm	1.0 cm	LF7	
24		-239.9 cm		Air	
26			45.0 cm		
27	Int. Image		45.0 cm		
28	Petzval III	239.9 cm	1.0 cm	LF7	
29		50.5 cm	9.5 cm	Air	
31	Petzval III	67.8 cm	2.2 cm	FK01	
32		-84.4 cm		Air	
34			34.3 cm		
35	Deformable			Mirror	
36			-73.4 cm	Air	
37				Mirror	
38			27.0 cm	Air	
39	Petzval IV	509.0 cm	1.0 cm	KZFSN	
40		72.4 cm	6.1 cm	Air	
42	Petzval IV	81.3 cm	19.1 cm	FK01	
43		-106.1 cm		Air	
45			52.7 cm		
47	Fold			Mirror	
49			106.0 cm	Air	
50	Parabola	203.0 cm		Mirror	-1.00
51			101.6 cm	Air	
52	Image				

6.3 Nominal Performance

The nominal performance of the two-Petzval system in terms of spot size is shown in table 6.2, and the radial encircled energy is plotted in figure 6.2. The three curves are for on-axis, half-field, and full-field. The spot sizes were calculated in a flat focal plane at the on-axis best focus. This gave a good indication of overall performance in the case of misalignments. If, for example, the spot sizes were given in independent field foci, it would be possible to have a system, with asymmetric and very strong field curvature or tilt, look good. The on-axis spot at best focus made comparing the performances of asymmetric systems easiest. There were slight variations between aligned performance in $\pm x$ - and y -fields because of the asymmetry of the off-axis focussing parabola following the last folding mirror.

Table 6.2. Performance of two-Petzval system.

Field	80% Encircled Energy
On - Axis	8.10 μm
+Y (α)	9.91 μm
-Y	9.91 μm
+X (β)	26.42 μm
-X	26.42 μm

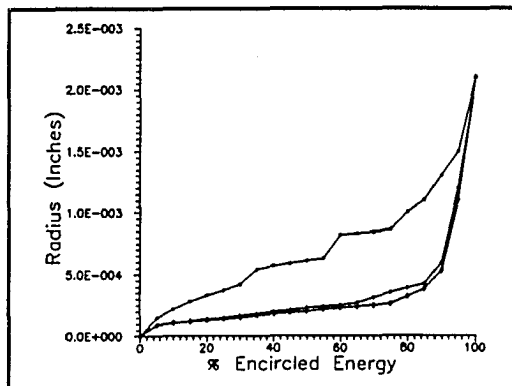


Figure 6.2. Two-Petzval nominal performance.

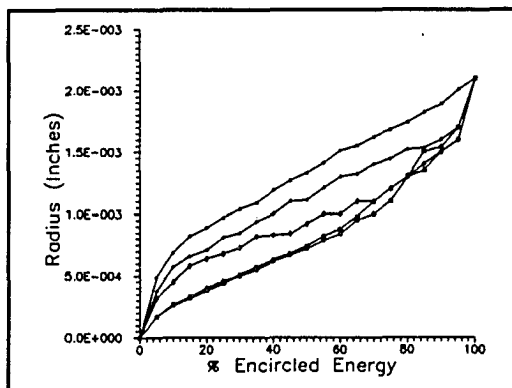


Figure 6.3. Misaligned two-Petzval performance.

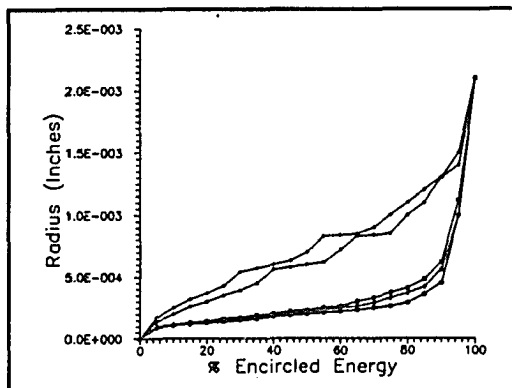


Figure 6.4. Realigned two-Petzval performance.

6.4 Misalignments Only

The alignment procedure was performed on the system with only misalignments present to evaluate the performance of the optimization method without any surface errors. The alignments of the model of the two-Petzval system were perturbed. The misalignment values are given in table 6.3. X-decenter of Petzval I and y-decenter of Petzval IV were included because the physical system allowed movement in these two degrees of freedom and line-of-sight was adjusted with the field compensating mirror rather than these lenses. The spot sizes of the misaligned system are given in table 6.4 and the resulting encircled energy can be seen in figure 6.3. The five curves are on-axis, $\pm y$ -fields (half-field), and $\pm x$ -fields (full-field). The misalignments were random, but large enough to degrade the system performance a noticeable amount.

Table 6.3. Misalignments of two-Petzval telescope.

Surface	Variable	Misalignment
9	X Decenter	-1.3 mm
22	X Decenter	3.8 mm
30	α Tilt	0.50°
30	β Tilt	0.25°
30	Y Decenter	1.3 mm
41	α Tilt	-0.25°
41	β Tilt	0.10°
41	Y Decenter	2.5 mm

Table 6.4. Performance of misaligned two-Petzval telescope.

Field	Nominal Alignment 80% Encircled Energy	Misaligned 80% Encircled Energy
On - Axis	8.10 μm	32.00 μm
+Y (α)	9.91 μm	33.27 μm
-Y	9.91 μm	33.02 μm
+X (β)	26.42 μm	38.61 μm
-X	26.42 μm	44.20 μm

The model system was optimized allowing the change of eight of the alignment variables of the Petzval elements. The targets were the 100 OPD's of the 20 rays shown in figure 6.5, evaluated in 5 fields. These values were found by raytracing through the model misaligned system. Raytracing is equivalent to perfect interferometry. The optimization could align the system with fewer targets, but this number was used to maintain consistency throughout the two-Petzval experiments. The positions of the target rays are not critical. A square grid of points was chosen to give an even sampling of the mirror surfaces. The corners of the square are cut as the points of the square fall outside of the entrance pupil.

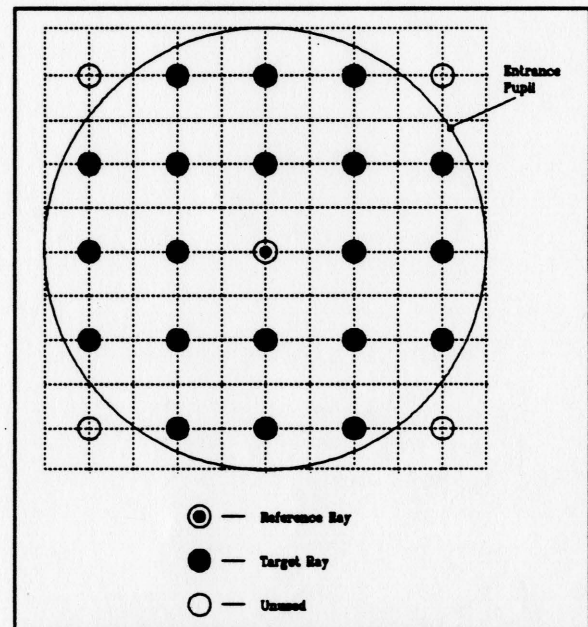


Figure 6.5. Rays used in optimization.

The variables optimized to the configuration given in table 6.5, column 4. Subtracting the alignment values of the optimized model from the alignment values in the original system under test, as would be done physically in an alignment iteration, gave the residual misalignment values in column 5. The resulting spot sizes are given in table 6.6, and the radial encircled energies in figure 6.4. The system returned to almost perfect performance. The remaining aberrations due to the residual element misalignments produce a slight astigmatism. The performance of the realigned system had a slight asymmetry in both x- and y-directions of approximately the same magnitude.

Table 6.5. Realignment of the two-Petzval telescope.

Surface	Variable	Misalignment	Optimized	Residual
9	X Decenter	-1.3 mm	0.0 mm	-1.3 mm
22	X Decenter	3.8 mm	1.6 mm	1.6 mm
30	α Tilt	0.50°	0.48°	0.02°
30	β Tilt	0.25°	0.34°	-0.09°
30	Y Decenter	1.3 mm	1.8 mm	-0.5 mm
41	α Tilt	-0.25°	-0.23°	-0.02°
41	β Tilt	0.10°	0.19°	-0.09°
41	Y Decenter	-2.5 mm	-2.8 mm	0.3 mm

Table 6.6. Performance of realigned two-Petzval telescope.

Field	Perfectly Aligned 80% Encircled Energy	Misaligned 80% Encircled Energy	Realigned 80% Encircled Energy
On-Axis	8.10 μm	32.00 μm	7.37 μm
+Y (α)	9.91 μm	33.27 μm	10.41 μm
-Y	9.91 μm	33.02 μm	9.40 μm
+X (β)	26.42 μm	38.61 μm	27.18 μm
-X	26.42 μm	44.20 μm	26.16 μm

6.5 Testing for Deformation of One Surface

The two-Petzval system was designed with two of the folding flats, surfaces 15 and 35, as deformable mirrors. The reverse optimization method was applied to detecting deformations in these elements. For the purpose of simulation, these mirrors could be represented as a grid of points, with the intermediate surface fit by cubic splines, a feature of the AccosV¹⁴ software.

For the first simulation, a $0.65\ \mu\text{m}$, approximately 1 wave, bump was placed on surface 15, the first deformable surface, at $(x/r, y/r) = (-0.43, -0.43)$ cm. The surface was modelled for data taking in AccosV as an 8×8 spline grid with all the other data points set to zero height. Representations of the surface are shown in figures 6.6 and 6.7. The contours are $0.13\ \mu\text{m}$, and the vertical scale of the surface plots is 1:50,000. The effects of the deformation on system performance are shown in table 6.8. There were however no misalignment errors present in this test. In order to simulate an unknown deformation in the surface under test, the spline grid for the deformation and the spline grid for the optimization were not identical

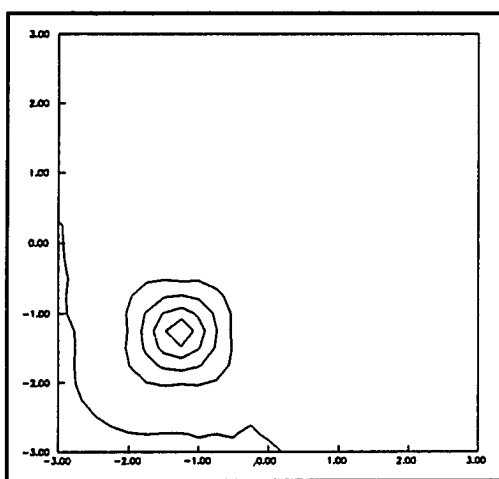


Figure 6.6. Initial deformation, surface 15.

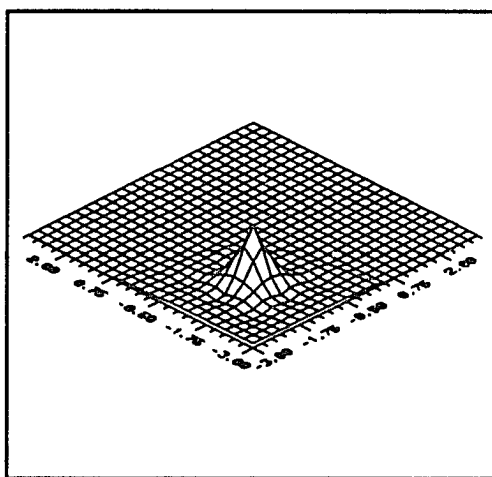


Figure 6.7. Initial Deformation, surface 15.

nor of harmonic frequencies. For the experiment with the 8x8 data, a 9x9 spline grid was used on surface 15.

OPD measurements produced by raytracing in AccosV¹⁴, in the grid shown in figure 6.5, were used as data for the experiment. There were five data sets, one for each of the five fields. The variables in this experiment were the 81 surface heights in the 9x9 grid and the focus term in each of the five fields.

The surface contour resulting from the optimization can be seen in figures 6.8 and 6.9. There was some compensation between the defocus variables and curvature in surface 15. The deformation stands out very clearly and was $0.66\ \mu\text{m}$ in height at $(x/r, y/r) = (0.5, 0.5)$. The contour plot showed some artifacts of the 9x9 grid.

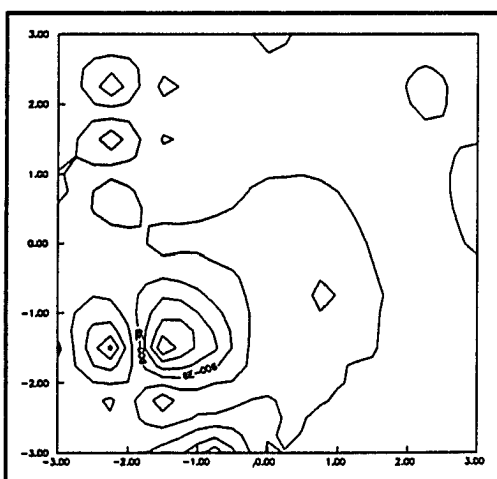


Figure 6.8. Optimized surface 15.

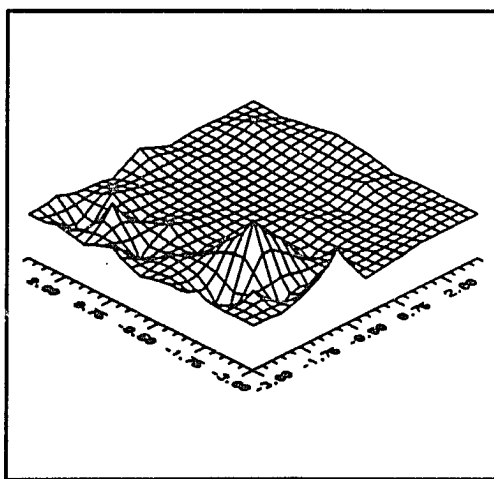


Figure 6.9. Optimized surface 15.

6.6 Testing for System Misalignments and Deformation of One Surface

The experiment was repeated, combining misalignments and surface deformation. It is important to consider the performance of the realigned system vs. the performance of the system with the deformations present. The initial misalignments were the same as the alignment only case, and the deformation was the same as in the one deformed surface test. The magnitudes of misalignments and deformation were chosen to have approximately the same order of effect on performance.

The variables were the 9x9 grid, and the tilt, decenter, and focus variables from the first simulation. The targets were the OPD data from raytracing the system with deformation and misalignments. The spline surface variables were damped, at 0.25 μm per increment, to diminish the effects of compensation with the focus and tilt variables. Jeong and Lawrence⁸ suggested setting three points on the surface being tested to zero height in order to establish a plane. In our special case of not adjusting the alignments of the mirrors being tested, this

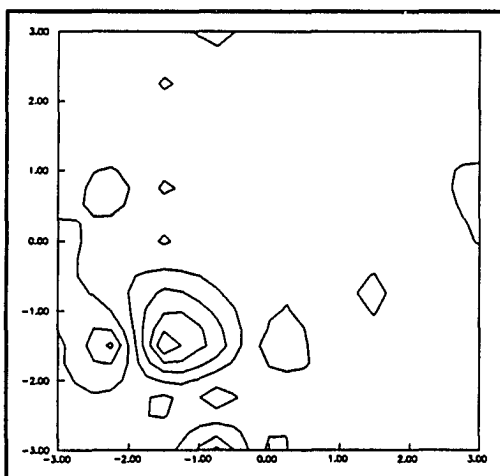


Figure 6.10. Optimized surface 15, with misalignments.

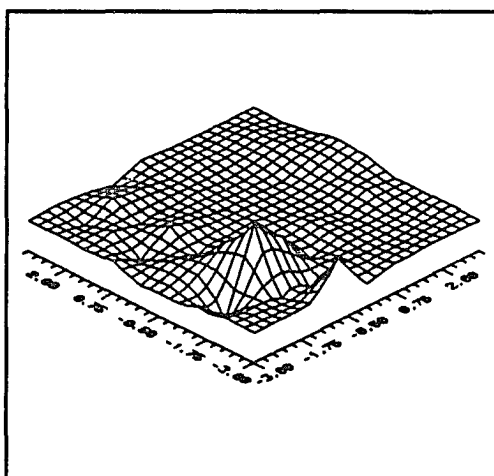


Figure 6.11. Optimized surface 15, with misalignments.

was not applicable.

The optimization of the alignment variables resulted in the alignments given in table 6.7, and the surface represented in figures 6.10 and 6.11. The deformation was clearly visible in the plots. The height of the deformation at $(x/r, y/r) = (-0.5, -0.5)$, the point closest to $(-0.43, -0.43)$ was $0.67 \mu\text{m}$, very close to the original deformation height.

The realignment based on the misalignment optimizations returned the system performance to very near that of the aligned system. The RMS wavefront errors are given in table 6.8. The surface deformation had lowered the performance of the aligned system, therefore the performance of the realigned system could only improve to the level of the original performance.

Table 6.7. Realignment with one surface deformation.

Surface	Variable	Misalignment	Optimized	Residual
9	x decenter	-1.3 mm	0.0 mm	-1.3 mm
22	x decenter	3.8 mm	2.3 mm	1.5 mm
30	α tilt	0.50°	0.33°	0.17°
	β tilt	0.25°	0.38°	-0.13°
	y decenter	-1.3 mm	0.5 mm	-1.8 mm
41	α tilt	-0.25°	-0.25°	0.00°
	β tilt	0.10°	0.16°	-0.06°
	y decenter	-2.5 mm	-2.5 mm	0.0 mm

Table 6.8. Performance of realigned telescope with one surface deformation.

Field	Aligned Performance	Misaligned Performance	Realigned Performance
On-axis	0.267 waves	0.625 waves	0.265 waves
+Y	0.229 waves	0.426 waves	0.201 waves
-Y	0.301 waves	0.874 waves	0.314 waves
+X	0.549 waves	0.826 waves	0.616 waves
-X	0.445 waves	1.210 waves	0.491 waves

6.7 Testing of Misalignments and Deformation of Two Surfaces

In the same manner that the effects of the misalignments of multiple surfaces were separated by the use of several field points, the effects of surface deformation could also be distinguished.⁸

The system under test was modelled with deformations of $0.64 \mu\text{m}$ at $(x/r, y/r) = (-0.43, -0.43)$ on surface 15, and $0.51 \mu\text{m}$ at $(0.2, 0.2)$ on surface 35. The deformable surfaces were modelled as 8×8 spline grids. The elements had the same misalignments as in the previous cases. The input surfaces are shown in figures 6.13-16. The deformation on surface 35 was wider than that of surface 15 because, while there was an 8×8 grid on both surfaces, surface 35 had a larger diameter to avoid vignetting.

Surfaces 15 and 35 of the model to be optimized were defined as two 9×9 grids. There was a software limit of two hundred variables that could be used in the optimization. Two 9×9 surfaces resulted in 162 variables. The largest values possible were chosen to give the highest sampling rate and reduce aliasing. In order to accommodate the larger number of variables, the number of rays per field was increased to 36, providing a total of 180 rays. The pattern is shown in figure 6.12.

The results of optimization of the alignment variables are given in table 6.9 with performance given in table 6.10. Performance improved to nearly that of the original system with deformations. The resulting surface optimizations are shown in figures 6.17-20. The deformation in surface 15 is clear. The optimization of surface 35 was noisier, due in part to the fact that the bump was not as near to a point on the 9×9 grid as in the case of surface 15.

Table 6.9. Optimization of misalignments and two surface deformations.

Surface	Variable	Misalignment	Optimized	Residual
9	x decenter	-1.3 mm	0.0 mm	-1.3 mm
22	x decenter	3.8 mm	2.0 mm	1.8 mm
30	α tilt	0.50°	0.18°	0.32°
	β tilt	0.25°	0.43°	-0.18°
	y decenter	-1.3 mm	0.8 mm	-2.1 mm
41	α tilt	-0.25°	-0.21°	-0.08°
	β tilt	0.10°	0.26°	-0.16°
	y decenter	-2.5 mm	-2.4 mm	-0.1 mm

Table 6.10. Performance of realigned telescope with deformations.

Field	Aligned Performance	Misaligned Performance	Realigned Performance
On-axis	0.473 waves	0.858 waves	0.463 waves
+Y	0.327 waves	0.538 waves	0.282 waves
-Y	0.324 waves	0.805 waves	0.271 waves
+X	0.464 waves	0.814 waves	0.608 waves
-X	0.422 waves	1.120 waves	0.481 waves

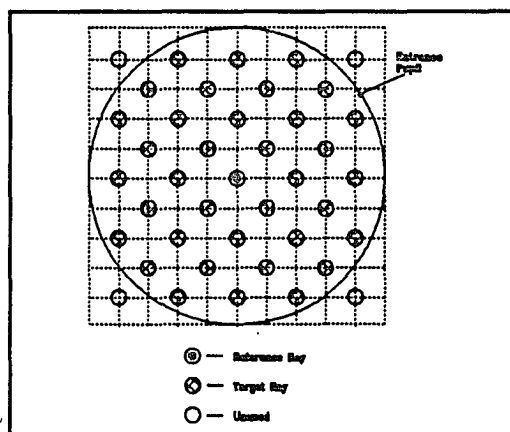


Figure 6.12. Rayset for optimization.

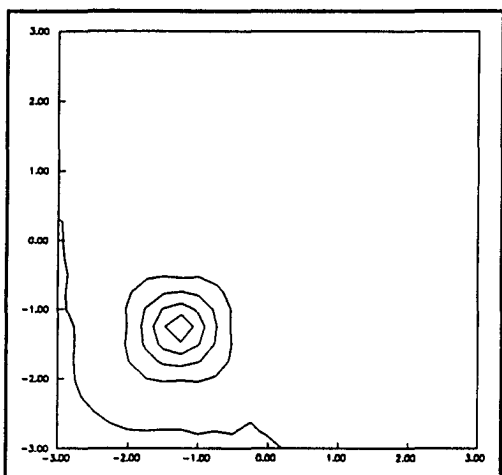


Figure 6.13. Initial deformation, surface 15.

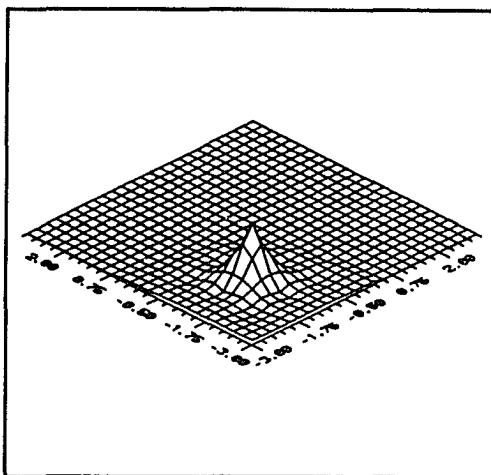


Figure 6.14. Initial deformation, surface 15.

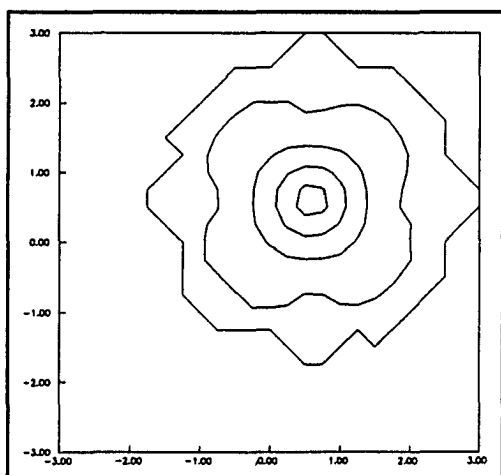


Figure 6.15. Initial deformation, surface 35.

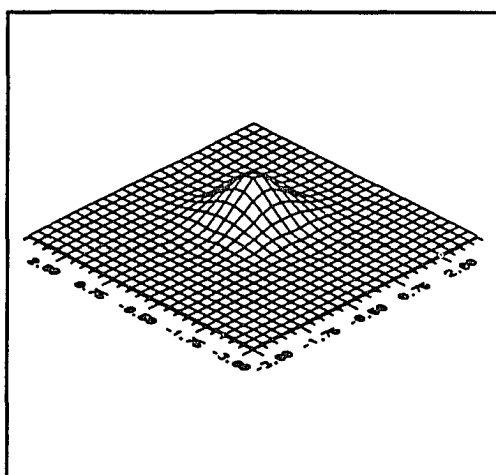


Figure 6.16. Initial deformation, surface 35.

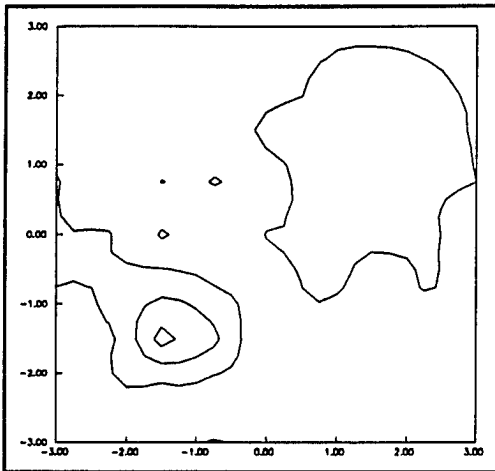


Figure 6.17. Optimized surface 15.

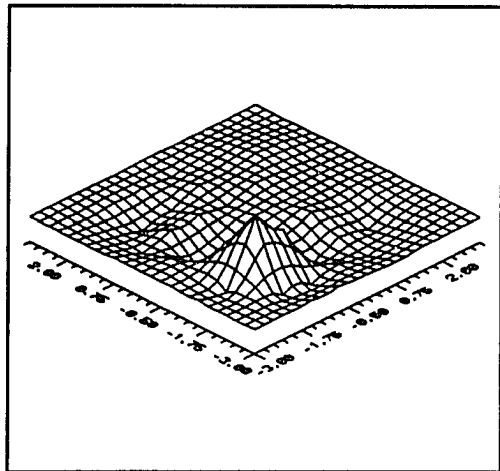


Figure 6.18. Optimized surface 15.

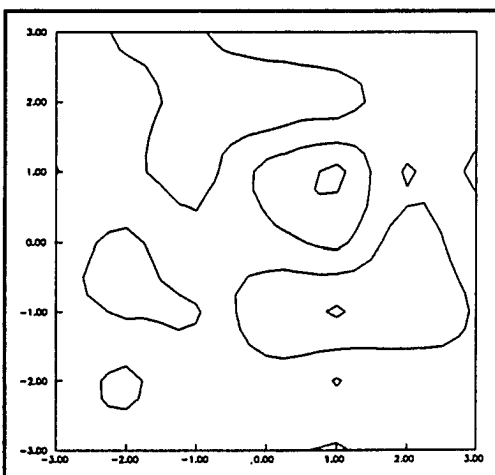


Figure 6.19. Optimized surface 35.

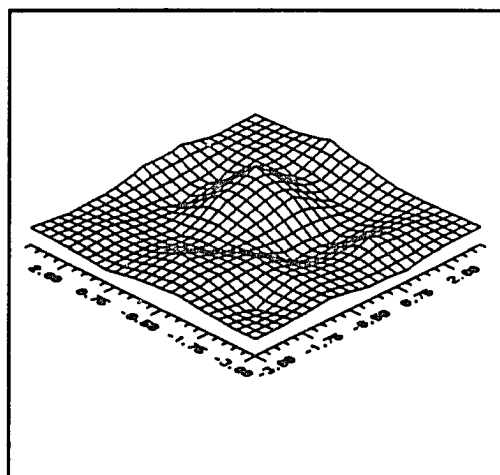


Figure 6.20. Optimized surface 35.

6.8 Conclusion

The limits on surface optimization included measuring ability, the resolution of the interferometer, and the nominal system performance. The practical limit was the number of optimization variables that could be used. With increasing number of variables, the time for optimization increased and eventually there was a hardware or software limit on the technique. The version of AccosV¹⁴ that was used allowed 200 variables, which for two surfaces and 15 alignment variables, left about 85 variables per surface. Because the splines were in a square array, the 9x9 grids provided the largest number of surface points.

It was possible to perform tests that simultaneously measure individual surface figure and misalignments of the elements of an optical system. It is advantageous to do so, assuming a computer-aided alignment method is used on the system. Figure errors interfere with the alignment process. While it is only possible to align a system with deformed surfaces to improve performance to the level allowed by the deformations, the deformations can be detected and if possible, corrected.

CHAPTER 7

EFFECTS OF GAUSSIAN NOISE ON THE OPTIMIZATION PROCESS

7.1 Introduction

The effects of noisy data on the performance of the reverse optimization process were investigated. The simulations provided random round-off error, but the simulated gaussian noise was a more realistic test. The Zygo interferometer of the OPTECAL testbed had a theoretical noise of 0.02 waves at $0.633 \mu\text{m}^{18}$. Noise of approximately this level was used in the simulations.

7.2 Simulations

The data from the alignment only simulation on the two-Petzval system was used as a base for the noise tests. The data had a round-off error of $0.04 \mu\text{m}$, 0.06 waves. The standard deviation for a flat distribution is $d/12$ where d is the distribution width. The σ of the round-off error was therefore 0.005 waves, an order of magnitude less than the simulated gaussian noise.

A computer program, listed in Appendix B, was used to add simulated gaussian noise to the base data of the alignment tests with σ equal to 0.00, 0.01, 0.02, 0.05, 0.10 and 0.25 waves. The results of optimizing the system with this data are shown in table 7.1. The effect on the optimization process can be seen in figure 7.1.

As noise increased, the system optimized to a higher merit function. Although this trend indicated a decrease in the ability to improve system performance, there was no noticeable change in the realigned performance up to 0.25 waves of noise, as shown in figure 7.2. This was a surprising result. The reason for the consistent performance level was the

number of optimization targets. The 100 targets used in the optimization were approximately a factor of five more than the number necessary to optimize the system. This provided an effective averaging out of the target noise.

Table 7.1. Performance of telescope realigned with noisy data, case 1.

Field	$\sigma = 0$ waves RMS OPD	$\sigma = 0.05$ waves RMS OPD	$\sigma = 0.25$ waves RMS OPD
On-Axis	0.059 waves	0.063 waves	0.050 waves
+Y	0.115 waves	0.113 waves	0.121 waves
-Y	0.114 waves	0.110 waves	0.130 waves
+X	0.423 waves	0.432 waves	0.411 waves
-X	0.423 waves	0.433 waves	0.397 waves

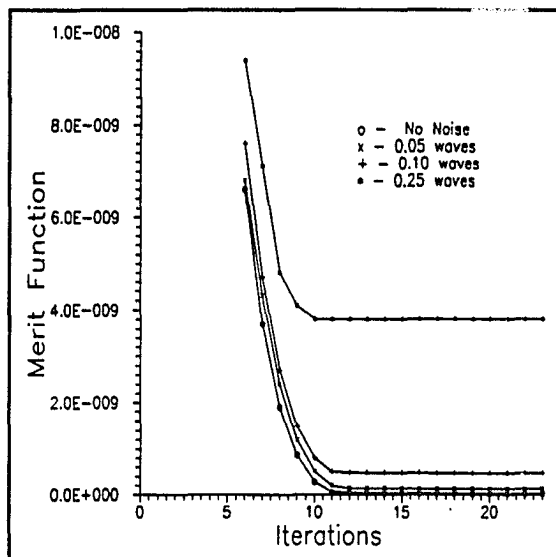


Figure 7.1. Effects of noise on optimization.

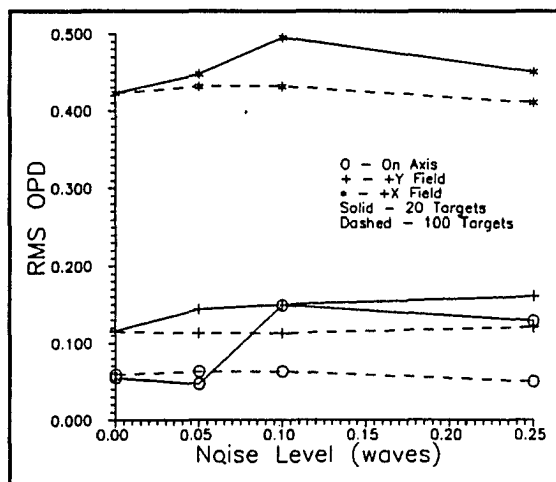


Figure 7.2. Effects of noise and target number on realigned performance.

A second experiment was conducted, using only twenty targets in the optimization. The same data set was used, but leaving out eighty of the targets. Table 7.2, column 2, optimization with no noise, indicates that this number of targets was sufficient to realign the system with no noise. The larger number of targets had been used in the experiments with figure error.

The performances of the realigned systems is shown in table 7.2. The progress of the optimizations was similar to the case of 100 targets, but the performance gets worse with increasing noise, as shown in figure 7.2. In some cases the simulations failed to optimize. The same optimization with 100 variables still worked well, but with only 20 targets, the optimization froze. This indicates that with few targets, a "lucky" amount of noise can cause problems with the optimization. We would expect to get cases where the 100 target case did not work, but none were observed in the limited sample.

Table 7.2. Performance of telescope realigned with noisy data, case 2.

Field	$\sigma=0.00$ waves RMS OPD	$\sigma=0.01$ waves RMS OPD	$\sigma=0.05$ waves RMS OPD	$\sigma=0.10$ waves RMS OPD	$\sigma=0.25$ waves RMS OPD
On-Axis	0.055 waves	0.055 waves	0.047 waves	0.149 waves	0.129 waves
+Y	0.116 waves	0.118 waves	0.144 waves	0.150 waves	0.161 waves
-Y	0.093 waves	0.093 waves	0.094 waves	0.159 waves	0.187 waves
+X	0.423 waves	0.428 waves	0.448 waves	0.496 waves	0.451 waves
-X	0.441 waves	0.437 waves	0.432 waves	0.472 waves	0.393 waves

7.3 Conclusion

The reverse optimization method will break down under high enough noise levels. The process performed well, at wavefront noise levels up to 0.25 waves for the two-Petzval system. This falls within the achievable precision of many optical testing methods. It is not possible to generalize this result to other systems as the tolerable noise level for an individual optical system depends upon its performance requirements and the design itself. But, it is encouraging that the required test precision could have been met by common testing methods.

The sources of noise for a Hartmann-type test and an interferometric test are not all the same, but noise will be present in targets generated by either. We have stated that the wavefront measurement method made it easier to generate a large number of data points. This is an advantage when the data is noisy. Although the main advantage of high spatial sampling rate is the elimination of aliasing, a large number of targets in the optimization also cancels out some of the effects of noise.

CHAPTER 8

EXPERIMENTAL VERIFICATION

8.1 Introduction

Alignment experiments were performed on the OPTECAL¹⁰ testbed at RADC to demonstrate the feasibility of the wavefront alignment method. This was the first alignment method tested on the OPTECAL¹⁰. The testbed provided the opportunity for making controlled misalignments and wavefront measurements at multiple fields on a high quality optical system.

In preparation for testing the method of reverse optimization, the two-Petzval optical system was aligned conventionally and interferograms were made of the nominally aligned system.

The first experiment was to misalign the system in various, known ways and take data of these misaligned systems. The optimization would then be run, based on the data from these various states of alignment to see if the optimization matched the known misalignments.

8.2 Experimental Setup

The OPTECAL system, shown in figure 8.1, was designed to make three types of performance measurements on the two-Petzval optical system. These are double-pass interferometry, shearing (wavefront sensing) interferometry, and PSF measurements. The double-pass interferometer was used for the alignment experiments. The data were collected by computer and processed by the FRINGE² reduction program.

The experimental setup is shown in figure 8.1. A Zygo ZAPP III PSI, mounted on the testbed, provided interferometric data. The interferometer produced a converging beam which was relayed to the input off-axis parabola. The collimated beam was input to the two-Petzval system, described in Chapter 6. The output beam from this system could be tested in the shearing interferometer (wavefront sensor) or returned to the Zygo for double-pass measurements, depending on the position of the double-pass fold mirror. The line-of-sight was kept constant and tilt could be added to the system by use of the field compensation mirror.

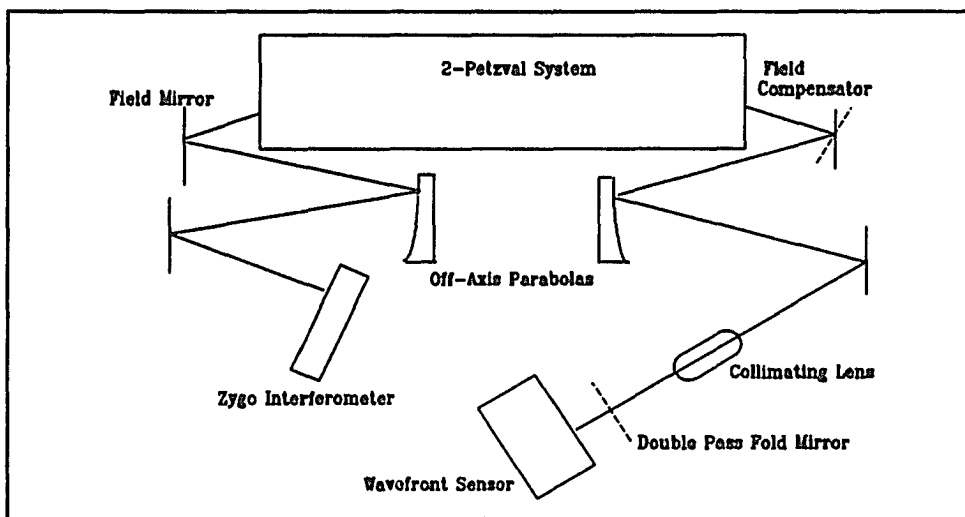


Figure 8.1. OPTECAL schematic diagram showing Zygo interferometer as light-source, the collimating and imaging parabolas, and the fold mirrors.

8.3 Pre-alignment

The first step in the pre-alignment was to measure the nominal aberrations in the test beam produced by the Zygo interferometer and the first parabola. This was done by tilting the field mirror normal to the beam in order to reflect the beam directly back into the input section and interferometer. The final RMS wavefront error, after some adjustments to the off-axis parabola, was 0.02 waves at 0.6328 μm .

The system performance was tested at the intermediate focus between Petzval II and III (see table 6.1). This was done by using a precision ball bearing as a negative element, at one radius of curvature distance from the intermediate focus. The system was tested in the five field positions that would be used for the alignment and surface measurement tests. The x-decenters of Petzval I and II were adjusted for the best possible wavefronts.

The entire system was tested double-pass, using the field compensating mirror as the return surface, and Petzval III then Petzval IV were adjusted to give the best performance possible.

8.4 Alignment Experiments

Ten interferograms were made in each field, the same fields as the two-Petzval model in Chapter 6. Ten were used to get an average, removing the effects of vibration or thermal air currents. The OPTECAL component actuators produced a large amount of heat.

Zernike polynomials were fit to the interferometric data, and the data averaged for each field. Focus, tilt, and piston were removed and OPD maps of the output wavefronts were generated. These OPD values at the points in figure 6.5 were then used as targets for optimization in the AccosV software.

The alignment variables used for the test were the same as in the alignment-only simulation described in Chapter 6. Simulation showed that it was necessary to damp the decenter of Petzval I, therefore this variable was damped in the optimization. Z-decenters of Petzval III and IV were added to the variable set, though these degrees of freedom were not perturbed in the tests. In the first attempted optimizations, there were some instabilities-- the alignment state would jump. This was solved by damping the decenters at 0.25 mm per increment and the tilts at 0.1 degree per increment.

Power was removed from the data during the Zernike-fitting in FRINGE, but it was necessary to allow the focus variables as the system is modelled with focus in a flat plane.

The amount of tilt in the measurements was unknown, therefore variables had to be constructed for this aberration. Tilt and piston were removed from the data in the process of Zernike-fitting in FRINGE². As the raytracing used in the AccosV¹⁴ software includes tilt due to element misalignment, and there is no simple way to automatically tilt the image

plane, it was necessary to add fifteen variables, three in each field, to simulate tilt and piston aberration. This was done by using "dummy" surfaces in the lens model to generate a tilt/piston wavefront which was added to the optimization targets. Figure 8.2, shows the "dummy" surfaces and the resulting OPD's added to the targets. The tilts required no damping, but the piston terms had to be damped at $2.5 \mu\text{m}$ per increment.

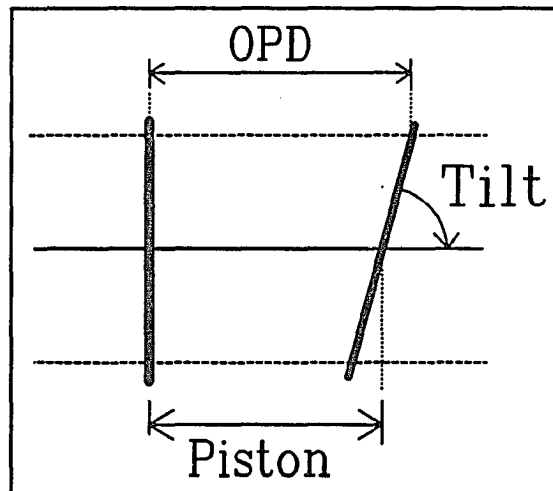


Figure 8.2. Simulating tilt and piston.

The nominal system data were used as targets in the reverse optimization process with the set of alignment variables described in section 8.1. Some misalignments of the elements were expected, as the nominally aligned system did not show perfect performance. The nominal misalignments as calculated by the reverse optimization test are shown in table 8.1, and the RMS wavefront errors, calculated by FRINGE, are given in table 8.2.

Table 8.1. Optimization of nominal misalignments.

Variables	Optimized
xd I (x decenter of Petzval I)	0.25 mm
xd II	1.02 mm
a III (α tilt of Petzval III)	0.13°
b III (β tilt of Petzval III)	0.01°
yd III (y decenter of Petzval III)	0.25 mm
a IV	-0.031°
b IV	0.03°
yd IV	0.00 mm

Real and simulated interferograms for three of the fields are shown in figures 8.3 - 8.8. The level of the contour lines shown is 1/10 wave. The nominally aligned two-Petzval system shows very good correspondence to the model system. As the experiment was designed to test change in the alignment and not absolute alignment, no corrections were made to the nominally aligned system. The alignment data on the nominal system were used to evaluate the optimizations of the misaligned states.

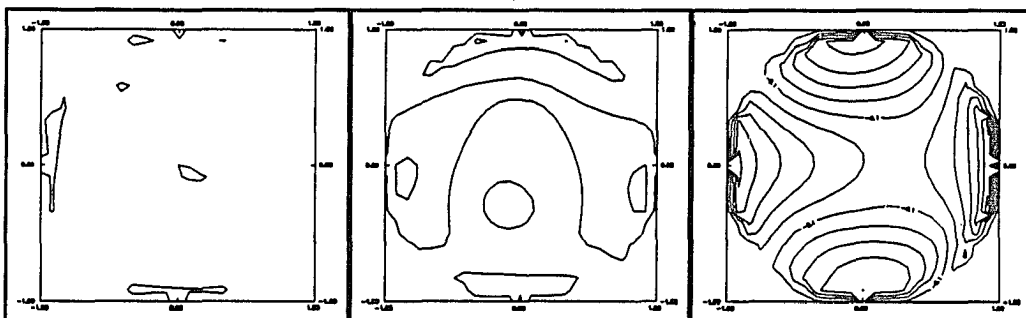


Figure 8.3.
OPTECAL on-axis.

Figure 8.4.
OPTECAL +Y-field.

Figure 8.5.
OPTECAL +X-field.

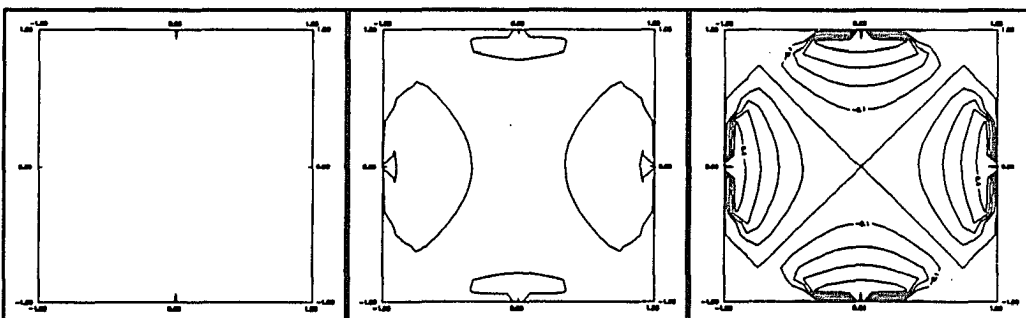


Figure 8.6.
Model on-axis.

Figure 8.7.
Model +Y-field.

Figure 8.8.
Model +X-field.

Table 8.2. Nominal RMS wavefront error of OPTECAL.

Field	Model RMS OPD (waves)	Measured RMS OPD (waves)
On - Axis	0.004	0.033
+Y	0.056	0.072
+X	0.225	0.240

8.4 Misalignments

Random misalignments of magnitudes that would noticeably effect performance were added to the system. The idea of the experiment was to see if the alignments could be calculated through the wavefront measurements and reverse optimization. As there was a measure of the nominal misalignment, given by the optimization of the aligned state, the ideal result of the misaligned optimizations would be the nominal misalignment, as measured by reverse optimization, plus the known change in alignment of each degree of freedom.

Experiments were performed using different combinations and magnitudes of misalignments. The reverse optimization calculated the set of misalignments given in tables 8.3, and 8.5. The residual errors can be viewed as the misalignments left in the system after one iteration, or the error in measuring change in the system. The bar graphs, figures 8.9 and 10, show the misalignments present in the system and the values to which the alignment variables optimized.

Table 8.3. Results of optimization, case 1.

Variable	Nominal	Change	Position	Optimized	Residual
x _d I	0.00 mm	0.00 mm	0.00 mm	0.25 mm	-0.25 mm
x _d II	1.02 mm	0.25 mm	1.27 mm	2.04 mm	-0.76 mm
alpha III	0.13°	0.53°	0.66°	0.36°	0.30°
beta III	0.01°	-0.26°	-0.25°	-0.25°	0.00°
y _d III	0.00 mm	0.25 mm	0.25 mm	0.75 mm	-0.50 mm
alpha IV	-0.03°	-0.26°	-0.29°	-0.23°	-0.06°
beta IV	0.03°	0.53°	0.56°	0.40°	0.16°
y _d IV	0.00 mm	0.00 mm	0.00 mm	1.00 mm	-1.00 mm

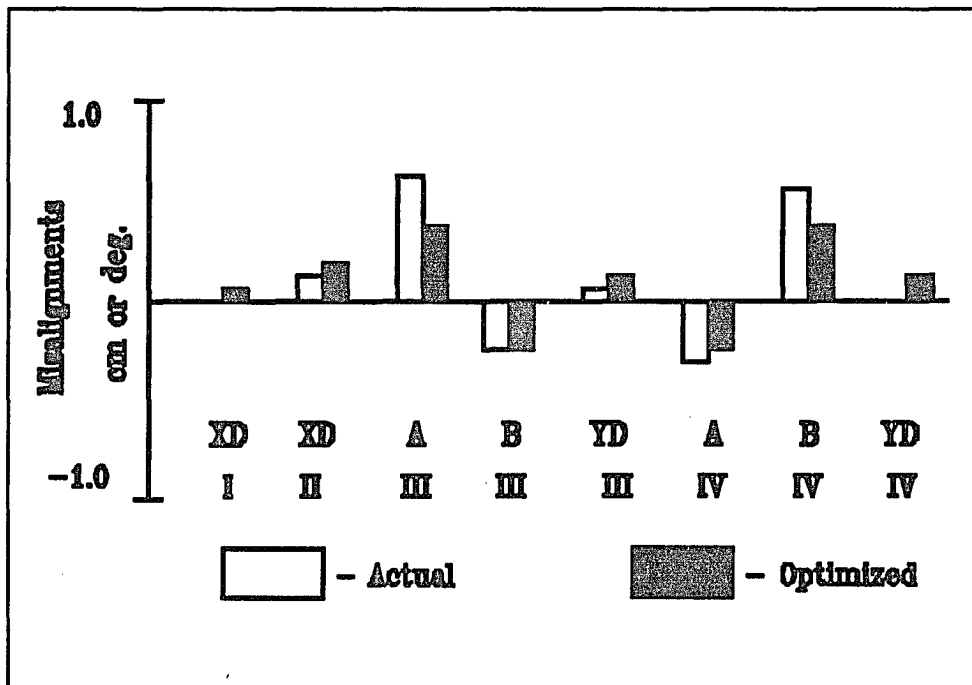


Figure 8.9. Actual and computed misalignments, case 1.

The OPTECAL system was perturbed by other research projects and it was necessary to establish a new nominal alignment state due to hysteresis involved in moving the table elements. The actual repeatability for each measurement of an actuator driven degree of freedom was $25 \mu\text{m}$ or 0.01° ¹⁸, but the table contained several non-actuator-controlled elements that could permanently change the alignment state. The optimization of the nominally aligned state is shown in table 8.4.

Table 8.4. New nominal state.

Variable	Optimized
xd I	0.25 mm
xd II	2.29 mm
alpha III	0.10°
beta III	-0.13°
yd III	0.25 mm
alpha IV	-0.05°
beta IV	0.12°
yd IV	0.25 mm

Another set of misalignments was induced in the elements and another optimization made, using the new nominal alignment values. The results of the optimization are shown in table 8.5 and figure 8.10.

Table 8.5. Results of optimization, case 2.

Variable	Nominal	Change	Position	Optimized	Residual
xd I	0.25 mm	0.25 mm	0.51 mm	0.25 mm	0.25 mm
xd II	2.29 mm	-0.25 mm	2.03 mm	3.30 mm	-1.27 mm
alpha III	0.10°	0.15°	0.25°	0.22°	0.03°
beta III	-0.13°	0.44°	0.31°	0.04°	0.27°
yd III	0.25 mm	0.00 mm	0.25 mm	0.51 mm	-0.25 mm
alpha IV	-0.05°	0.04°	-0.01°	-0.04°	0.03°
beta IV	0.12°	0.11°	0.23°	0.31°	-0.08°
yd IV	0.25 mm	0.00 mm	0.25 mm	0.51 mm	-0.25 mm

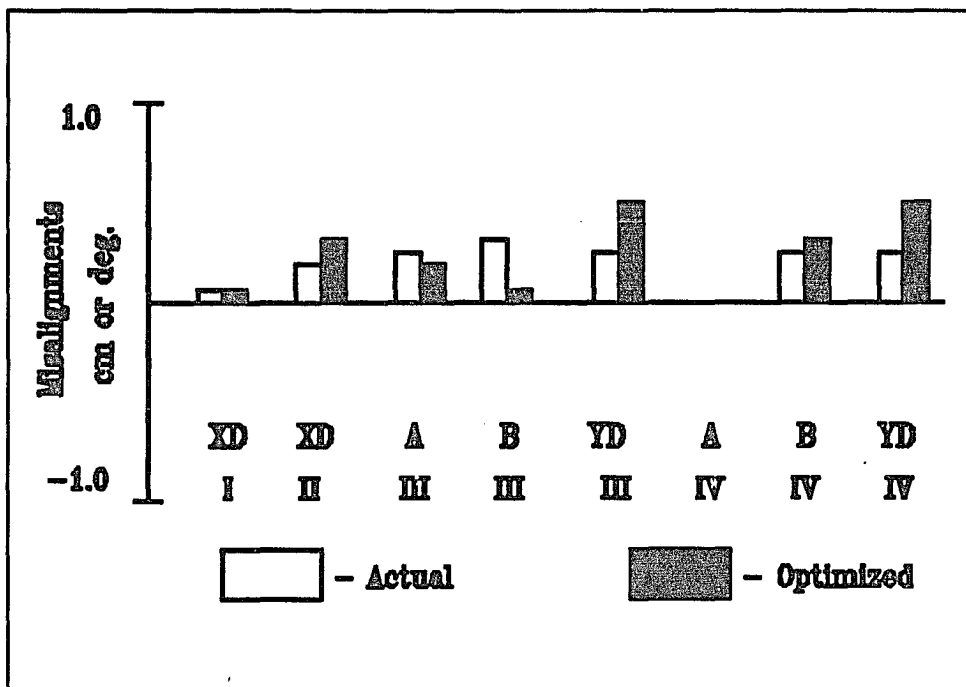


Figure 8.10. Actual and computed misalignments, case 2.

8.5 Conclusion

The experiments show a close correspondence of the optimization to the actual misalignments. While the OPTECAL system has very good control of the specified alignment variables of the two-Petzval system. There are degrees of freedom of folding flats, the parabolas, etc., which are not precisely controlled. This created some unknowns in the model system, resulting in less than perfect alignment corrections. It was not within the scope of these experiments to align every element on the table.

The alignment-only tests show that the reverse optimization process will work to improve the alignment of an optical system. In the ray aberration based realignments, approximately four iterations were required to maximize system performance. The wavefront method gave good corrections in one iteration. Unfortunately it was impractical to perform these tests with more than one alignment iteration or including surface deformations, so the full abilities of the method are unknown.

CHAPTER 9

CONCLUSION

9.1 Summary

Optical system designers have come to rely more heavily on computers for optical design and off-axis and other asymmetric types of lenses and mirrors have become more common. Computer controlled lens grinders have made the construction of these types of elements possible, but the testing and alignment are still difficult. Nulling techniques are costly and time consuming, and the nulling elements themselves need to be constructed, tested, and aligned.

Computer-generated holograms are useful in this type of testing. But, the quality of the holograms is a limiting factor on testing, especially at visible wavelengths. There is still the problem of aligning the source, test-piece, and hologram.

The process of reverse optimization can solve or help solve many of these problems. The wavefront aberration method can be used to test component figure as well as alignment. By testing the components end-to-end, in the system, the need for extra optical components is eliminated. The equipment required for the aberration measurements can be used on several systems, not just the immediate one.

9.2 Ray Aberration Method

A testbed was constructed to test the feasibility of ray-aberration-based reverse optimization and to apply the technique to an actual system. Several tests of alignment and performance were conducted, and the equipment and alignment procedures were refined.

The experiments done using the ray aberration approach to reverse optimization were successful in improving the alignment of the telescope. The ray approach is intuitively understandable, and relatively easy to set up, and adapt to different optical systems, but it was difficult to perform because of the measurement precision required. Another concern with the Hartmann test is that the experimental time increases with the number of rays used, the sampling frequency.

This method would be most useful with limited budget or when rough alignments of the system are desirable. The Hartmann type test can be used for systems in very bad starting misaligned states or with poor surface quality.

9.3 Wavefront method

The OPD method was developed out of the desire for surface figure testing. The mathematics for optimization for either test is the same, but the OPD method allows much easier, higher spatial sampling of the output wavefront than did measuring individual ray aberrations.

The simulations with the Cooke triplet showed that the reverse optimization process using wavefront aberration data works well on high-quality optical systems. The work also demonstrated the need for either good modelling of the systems to be aligned or the optimization of surface parameters along with misalignments.

The simulations with the two-Petzval system demonstrated another type of system that the reverse optimization process could successfully align. The simulations were done in preparation for laboratory experiments on the two-Petzval telescope. The work showed that

highly asymmetric surface errors could be detected on multiple surfaces in the presence of misalignments.

While it is possible to optimize surface figure using the ray-based approach of Chapter 2, the accuracy required, the measurement time, and the diffraction limits on sampling hinder this process. The OPD measurement method, with high spatial sampling rate, flexible choice of targets and manipulation of data, is desirable when modelling is unsure, or figure measurements are required. Interferometry becomes difficult in the presence of large nominal aberrations, poor surface quality, high stray light levels, or vibration.

9.4 OPTECAL Experiments

While not exhaustive, the OPTECAL experiments showed that reverse optimization with wavefront aberration data will work to correct misalignments. Accuracy in data collection was essential, and would be difficult to achieve in some cases.

9.5 Future Possibilities

As methods of reverse optimization, and computer-aided techniques in general, are applied to real-world problems, they will become more and more useful to the designers and builders of optical systems. In addition to the standard tolerancing done in design work, design may include studies of how the system would perform under a computer aided alignment technique. Data reduction software for PSI's and other performance measurement devices could incorporate modelling and optimization capabilities.

Future research could also include more thorough investigations into the trends of optimization. Examples include how compensating variables effect the optimization, analytical predictions of damping needed on the variables, and the actual numbers of rays and fields needed for aligning generalized optical systems. Zernike polynomial fitting of data and wavefront reconstruction should be investigated as means of reducing the effects of noise. Other non-interferometric tests such as Ronchii rulings could be applied to reverse optimization. Further lab work with high quality optical systems to investigate the applications of the reverse optimization method are also needed. The process should also be tested for applicability to further optical systems.

APPENDIX A

REVIEW OF OPTIMIZATION

When evaluating any optical system, a set of parameters is chosen to represent system performance. These are usually spot sizes in various fields, the ray or wavefront aberrations of specific rays traced through the system, or the Seidel aberrations of the system. In optimization processes, these parameters are called operands and their ideal values, targets. The set of mechanical parameters that can be adjusted to change the performance parameters of the system, lens shape factor, material, spacing etc., are variables. A sensitivity matrix, change table, for the system can be expressed as the matrix: $A_{ij} = d(\text{operand}_i) / d(\text{variable}_j)$ for each variable and operand in the system. The merit function is defined as the squared sum of the operands, an ideal solution having a merit function of zero.

The process of least square optimization finds an extremum which is a solution for the simultaneous differential equations expressed by the matrix. It is assumed that the extremum is a minimum. No maximum should exist as the system can be made infinitely bad. This is accomplished by calculating a solution vector, a partial derivative, of the merit function with respect to each variable. Each variable is then adjusted in the direction of the minimum merit function as would be done in an approximated differential. To avoid overcorrecting, the change in the variable is damped. This damping can be adjusted for each variable.¹⁸

The lens system starts out in its ideal state- aligned. The operands are ray aberrations, OPD, or other performance measurements from a misaligned system. When the optimization is performed, the performance of the system gets worse, to match the misaligned system, hence the term reverse optimization¹. The merit function is decreasing, but the performance

of the system is getting worse. If enough targets are used, the model system will converge to a duplicate of the actual misaligned system.

APPENDIX B
SOFTWARE FOR NOISE SIMULATION

AccosV generated data with only round-error in its ray-tracing routines. To evaluate the effects of noise, it was desirable to add noise to the data derived from ray-tracing. This program is designed to read an input file of targets for optimization, add Gaussian noise of the desired σ , and rewrite a new, noisy, target file. The noise is simulated by adding three pseudo-random numbers generated in BASIC and scaling to the correct σ and $\langle x \rangle^{19}$.

```
'Gaussian Noise program GNOIS18.BAS
'Designed to add gaussian noise to 90 point OPD files for AccosV
'Input file must be of form
'With 8 space data
'  $accosv
'  av
'  n
'  lib get #
'  (rayset)
'  (definitions)
'  (variables)
'  requests
'  cfg,1
'  ol,#.....
'  cfg,2
'  ol,#.....
'Initialize Random Generator
line1:
  r = VAL(RIGHT$(TIMES$, 2)) * VAL(MID$(TIMES$, 4, 2))
  IF r = 0 THEN GOTO line1
  RANDOMIZE (r)
'Set up I/O files
  INPUT "Name of command file to add noise to: ", file$
  INPUT "Output file: ", fileN$
  OPEN file$ FOR INPUT AS #1
  OPEN fileN$ FOR OUTPUT AS #2
'Get sigma of data
  INPUT "Input Standard Deviation (waves) to Use: ", sigma
  sigma = sigma * (1 / 25.4) * (.001) * .6328
```

```
'Read off beginning of command data
  FOR i = 1 TO 8
    LINE INPUT #1, dup$
    PRINT #2, dup$
  NEXT i

'Go through 5 fields
  FOR j = 1 TO 5
    LINE INPUT #1, field$
    PRINT #2, field$
    FOR i = 1 TO 18
      LINE INPUT #1, dat$
      num$ = RIGHT$(dat$, 8)
      num = VAL(num$)
'ROUTINE for inducing NOISE
      y1 = RND
      y2 = RND
      y3 = RND
      nnum = num - (3 * sigma) + (2 * sigma * (y1 + y2 + y3))

'Get noisy data into output file
      count = LEN(dat$) - 8
      ope$ = LEFT$(dat$, count)
      out$ = ope$ + STR$(nnum)
      PRINT #2, out$
    NEXT i
  NEXT j
'Read off last of command data
  WHILE NOT EOF(1)
    LINE INPUT #1, dup$
    PRINT #2, dup$
  WEND
CLOSE
END
```

APPENDIX C
OPTIMIZATION TECHNIQUES

C.1 General Data Form

Each target represents the OPD between the traced ray and the reference ray. The numbers correspond to each ray in the grid shown in figure 6.5, Chapter 6, beginning in the upper right-hand corner. "cfg,#" is the configuration in the AccosV model. Each configuration corresponds to one field, "cfg,1" is the on axis field, "cfg,2", the +Y etc.

Table C.1. Sample data for optimization (AccosV).

Ray Number	On Axis OPD(waves)	+Y Field OPD(waves)	-Y Field OPD(waves)	+X Field OPD(waves)	-X Field OPD(waves)
2	-2.25	-1.74	-3.07	-2.42	-4.20
3	-1.73	-0.89	-2.83	-1.86	-3.76
4	-1.71	-0.40	-3.23	-0.61	-4.97
6	-1.04	-1.17	-1.54	0.48	-3.60
7	-0.40	-0.36	-0.65	-0.20	-1.25
8	-0.28	-0.08	-0.57	-0.32	-0.77
9	-0.20	0.20	-0.81	0.61	-1.70
10	0.32	0.93	-0.89	3.07	-3.56
11	0.08	-0.04	-0.67	2.06	-2.82
15	1.17	1.21	0.61	3.31	-1.21
16	2.83	0.93	-0.93	3.07	-3.60
17	0.08	0.53	-0.48	0.93	-1.41
18	0.00	0.24	-0.24	0.00	-4.85
19	0.53	0.57	0.28	0.73	-0.32
20	0.04	1.98	1.62	3.56	-0.44
22	0.65	1.90	-0.97	1.74	-2.67
23	0.73	1.62	-0.36	0.61	-1.25
24	1.66	2.22	0.81	1.45	-0.32

C.2 AccosV Optimization

The rayset used for optimization in AccosV is given in table C.2. Another grid at the $\pm 0.6, \pm 0.2$ was added to get the 36 element rayset.

Table C.2. Rayset for AccosV optimization.

Command	Number	Y	X	Comment
FOB	1	0	0	On-axis
RAY	1	-0.8	-0.8	Not used
RAY	2	-0.8	-0.4	
RAY	3	-0.8	0.0	
RAY	4	-0.8	0.4	
RAY	5	-0.8	0.8	Not used
RAY	6	-0.4	-0.8	
RAY	7	-0.4	-0.4	
RAY	8	-0.4	0.0	
RAY	9	-0.4	0.4	
RAY	10	-0.4	0.8	
RAY	11	0.0	-0.8	
RAY	12	0.0	-0.4	
RAY	13	0.0	0.0	Reference
RAY	14	0.0	0.4	
RAY	15	0.0	0.8	
RAY	16	0.4	-0.8	
RAY	17	0.4	-0.4	
RAY	18	0.4	0.0	
RAY	19	0.4	0.4	
RAY	20	0.4	0.8	
RAY	21	0.8	-0.8	Not used
RAY	22	0.8	-0.4	
RAY	23	0.8	0.0	
RAY	24	0.8	0.4	
RAY	25	0.8	0.8	Not used

For the simulations, tilt did not need to be corrected, therefore the DEFINITIONS commands took the form:

o(#) opd, (ray #)

For the experiments, the piston/ tilt term had to be added to the targets. In this case, AccosV would allow only 96 targets, as that was the limit on composite variables. Rays 12 and 14 were left out. The DEFINITIONS command for one operand was of the form:

oo(ray #) OPD, (ray #)

ooo(ray #) OPL, (ray #) (dummy surface #)

COM o(ray #)

ADD oo(#)

ADD ooo(#)

The resulting targets were named o(ray #).

The REQUEST set for AccosV was of the form:

CFG, (configuration #)

o(first ray #), (OPD value)...

...o(last ray #), (OPD value)

CFG, (next configuration #)

The tilt, thickness, decenter and asymmetric spline variables were of the normal AccosV form, weighted appropriately. The piston/ tilt correction variables were the tilts of one dummy surface and the thickness of another.

C.3 Super Oslo Optimization

The rayset used in Super Oslo is given in table C.3.

Table C.3. Rayset for optimizations in Super Oslo

Ray	Y	X
2	1.0	0.0
3	-1.0	0.0
4	0.0	1.0
5	0.0	-1.0
6	0.6	0.6
7	-0.6	-0.6
8	-0.6	0.6
9	0.6	-0.6
10	0.7	0.0
11	-0.7	0.0
12	0.0	0.7
13	0.0	-0.7

The operands used in Super Oslo were of the form:

O # OPD(ray #, 0, field #) - (Target).

REFERENCES

1. Hwan Joo Jeong, George N. Lawrence, and Kie B. Nahn, "Auto-alignment of a three-mirror, off-axis telescope by reverse optimization and end-to-end aberration measurements," SPIE, vol. 818, Current Developments in Optical Engineering II, San Diego, p 418, 1987.
2. FRINGE, University of Arizona
3. WISP, trademark of WYKO Corp.
4. K.P. Thompson, "Aberration fields in tilted and decentered systems", Phd Dissertation, University of Arizona, 1980
5. George N. Lawrence, Weng W. Chow, "Wave-front tomography by Zernike polynomial decomposition", Optics Ltrs., vol. 9, no. 7, 1984
6. J.W. Figoski, T.E. Shrode, G.F. Moore, "Computer-aided alignment of a wide-field, three-mirror, unobscured, high-resolution sensor", to be published in SPIE Proc., 1049
7. ALI, Code V, Trademarks of Optical Research Assoc.
8. Hwan J. Jeong, George N. Lawrence, "Simultaneous determination of misalignment and mirror surface figure error of a three mirror off-axis telescope by end-to-end measurements and reverse optimization : numerical analysis and simulation", SPIE 966 46, San Diego 1988
9. Steve Wong, "Fringe analysis for testing optical surfaces", SPIE code no. 966-53
10. K.M. Magde, T.J. Heydenburg, J. Killius, "An optical testbed for control algorithms (OPTECAL)", SPIE vol. 965, Current Developments in Optical Eng. III, pp 162-167, (1988)
11. I. Ghozeil, "Hartmann and Other Screen Tests", in Optical Shop Testing, D. Malacara ed., pp 323-349, John Wiley and Sons, Inc., 1978
12. LaDiTe, Trademark of WYKO Corp.
13. Brian O. Kelly, "Lateral-Effect Photodiodes", Laser Focus, pps 38-40, Mar. 1976
14. AccosV, trademark of Harris: Scientific Calculations
15. Super Oslo, trademark of Sinclair Optics
16. Cooke Triplet, Sinclair Super Oslo Library, SO_TRPLT (demo)
17. "Adaptive Simulation Software User's Guide: Att. V to OPTECAL Final Report", Hughes Aircraft Co.

18. "Final Technical Report: OPTECAL", RADC-TR-88-202, vol. I, Hughes Aircraft Co.
19. "OPTECAL Interim Report", vol. III, Apr 1987, EDSG Report FR-87-77-540, Hughes ref #f6782
20. "Least Squares Optimization", Chapter 9, Super Oslo Manual, Sinclair Optics
21. B. Roy Frieden, Probability, Statistical Optics, and Data Testing, pps 93-5, Springer-Verlag, 1983